

On the Hydrodynamic Interaction of Shock Waves with Interstellar Clouds. II. The Effect of Smooth Cloud Boundaries on Cloud Destruction and Cloud Turbulence

Fumitaka Nakamura^{1,2}, Christopher F. McKee^{3,4}, Richard I. Klein^{3,5}, Robert T. Fisher⁶

ABSTRACT

The effect of smooth cloud boundaries on the interaction of steady planar shock waves with interstellar clouds is studied using a high-resolution local adaptive mesh refinement technique with a second-order accurate axisymmetric Godunov hydrodynamic scheme. A three-dimensional calculation is also done to confirm the results of the two-dimensional ones. We consider an initially spherical cloud whose density distribution is flat near the cloud center and has a power-law profile in the cloud envelope. Our model can be specified by three model parameters: the power law index of the density profile (n), the density contrast (χ), and the Mach number of an incident shock relative to the sound speed of the preshock ambient medium (M). The evolution of the shocked cloud is divided into four stages: (1) the initial transient stage, in which the initial shock is transmitted to the cloud, and at the same time is reflected at the cloud surface to form a bow shock or bow wave; (2) the shock compression stage, in which the shocked cloud is compressed in the direction of shock propagation; (3) the postshock expansion stage, in which the cloud expands in the radial direction; and (4) the cloud destruction stage, in which the shocked cloud is shredded into small fragments and is eventually destroyed. This evolution is qualitatively consistent with previous simulations of shocks interacting with uniform clouds with sharp cloud boundaries. However, smooth cloud boundaries significantly affect the morphology of the shocked clouds and cloud destruction timescales. When an incident shock is transmitted into a smooth cloud, velocity gradients in the cloud envelope steepen the smooth density profile at the upstream side, resulting in a sharp density jump having an arc-like shape. We refer to this density jump as a “slip surface” because the velocity is sheared parallel to its surface. Such a slip surface forms immediately when a shock strikes a cloud with a sharp boundary. For

¹Faculty of Education and Human Sciences, Niigata University, 8050 Ikarashi-2, Niigata 950-2181, Japan

²Division of Theoretical Astrophysics, National Astronomical Observatory, Mitaka, Tokyo 181-8588, Japan

³Department of Astronomy, University of California, Berkeley, CA 94720

⁴Department of Physics, University of California, Berkeley, CA 94720

⁵Lawrence Livermore National Laboratory, P.O. Box 808, Livermore, CA 94550

⁶The ASC FLASH Center, The University of Chicago, 5640 S. Ellis, Chicago, IL 60637

smoother boundaries, the formation of slip surface and therefore the onset of hydrodynamic instabilities are delayed. Since the slip surface is subject to the Kelvin-Helmholtz and Rayleigh-Taylor instabilities, the shocked cloud is eventually destroyed in $\sim 3 - 10$ cloud crushing times, where the cloud crushing time is the characteristic time for the shock to pass through the cloud. The ratio of the cloud destruction time to the cloud crushing time depends mainly on the smoothness of the density profile and only weakly on the density contrast for strong shocks. We construct analytic models of cloud drag and vorticity generation that compare well with the numerical results. After complete cloud destruction (in several cloud crushing times), small blobs formed by fragmentation due to hydrodynamic instabilities have significant velocity dispersions of the order of $0.1 v_b$, where v_b is the shock velocity in the ambient medium. Our simulations show that, irrespective of the smoothness of the initial density profile, it is difficult to sustain the vortical motions inside the cloud because the cloud is being destroyed by hydrodynamic instabilities. This suggests that turbulent motions generated by shock-cloud interaction are directly associated with cloud destruction. The interaction of a shock with a cold H I cloud should lead to the production of a spray of small H I shreds, which could be related to the small cold clouds recently observed by Stanimirovic & Heiles (2005). We also calculate the dependence of the velocity dispersion (Δv) on region size (R), the so-called linewidth-size relation, based on a three-dimensional simulation. The linewidth-size relation obtained from our simulation is found to be time-dependent. In the early stages of cloud destruction, the small-scale fluctuations dominate because of the nonlinear growth of the Kelvin-Helmholtz instability, and thus the linewidth-size relation is more or less flat. In the later stages, the small-scale fluctuations tend to damp, leading to a linewidth that increases with size. A possibility for gravitational instability triggered by shock compression is also discussed. Only radiative shocks with $\gamma < 4/3$ can lead to induced gravitational collapse. We show that in the absence of significant nonthermal motions behind the shock, star formation can be induced in an initially uniform cloud by a radiative shock only if it is not too strong. Our results indicate that the postshock gas has significant nonthermal motions, and this can further limit the onset of gravitational collapse.

Subject headings: hydrodynamics — ISM: clouds — shock waves — supernova remnants — turbulence

1. Introduction

The interaction of shock waves with interstellar clouds is a very common event in interstellar medium (ISM). For example, supernova explosions produce large blast waves that propagate into the ISM. The blast waves strike interstellar clouds, compressing them and destroying them. This process plays an important role in the formation of multi-phase structures in the ISM (Cox &

Smith 1974; McKee & Ostriker 1977). Recently, several authors have proposed it as a mechanism for generating the supersonic turbulence observed in the ISM (e.g., Kornreich & Scalo 2000; MacLow & Klessen 2003; Vazquez-Semadeni et al. 2000). Compression by shocks may be able to trigger star formation in interstellar clouds (Elmegreen & Lada 1977). In the early universe, supernova explosions of the first stars may be responsible for the first significant generation of turbulence and the first metal enrichment in the intergalactic medium after the Big Bang. Other energetic events, such as stellar winds of massive stars, bipolar outflows of young stellar objects, cloud-cloud collisions, and spiral density waves can also produce interstellar shocks that interact with the surrounding clumpy ISM. Hence, understanding how shock waves interact with interstellar clouds is an important step in understanding the structure and evolution of the ISM.

Many authors have studied the interaction of shock waves with interstellar clouds, either analytically (e.g., McKee & Cowie 1975; Spitzer 1982; Heathcote & Brand 1983; McKee et al. 1987; Nulsen 1982) or numerically (Sgro 1975; Woodward 1976; Nittman et al. 1982; Tenorio-Tagle & Rozyczka 1986; Bedogni & Woodward 1990; Stone & Norman 1992; Klein, McKee & Colella 1990, 1994 (hereafter KMC), Mac Low et al. 1994; Dai & Woodward 1995; Xu & Stone 1995). Such calculations are closely related to the interaction of a cloud with a wind (KMC; Schiano, Christiansen, & Knerr 1995; Gregori et al. 2000). Analytic studies have focused mainly on the structure and evolution of a shock transmitted into a cloud before cloud destruction. After the shock passes through the cloud, hydrodynamic instabilities such as Rayleigh-Taylor, Richtmyer-Meshkov, and Kelvin-Helmholtz begin to develop and may eventually destroy the entire cloud. It is difficult to follow such highly nonlinear stages of evolution analytically, and thus numerical calculations are needed. KMC performed comprehensive two-dimensional numerical studies of the interaction of shocks with uniform clouds based on the adaptive mesh refinement (AMR) technique. They showed that small, nonradiative clouds are destroyed in several cloud crushing times, where the cloud crushing time is the timescale for a shock to propagate through the cloud (see §2 for the definition). They also demonstrated that good spatial resolution (at least 10^2 cells per cloud radius) is needed in numerical calculations in order to follow the cloud destruction accurately. Stone & Norman (1992), Klein & McKee (1994), and Xu & Stone (1995) performed three-dimensional numerical simulations on this problem, showing that overall evolution of the cloud destruction is in good agreement with the two-dimensional results of KMC, although vortex rings observed in the two-dimensional calculations are unstable in three dimensions and the cloud destruction proceeds more violently in all directions.

Recently, Klein et al. (2000, 2003) performed a series of Nova laser experiments investigating the evolution of a high density sphere embedded in a low density medium after the passage of a strong shock (with a Mach number of ~ 10). The results of these experiments can be compared directly with interstellar shock-cloud interaction under certain scale transformations (Ryutov et al. 1999). The comparison of their experimental results with two-dimensional simulations can reproduce the morphological evolution of the experimental shocked spheres reasonably well. In later stages of cloud destruction, the three-dimensional instability of vortex rings plays a significant role,

and fully three-dimensional calculations are required to follow the evolution. Follow-up experiments on the Omega laser confirmed the presence of vortex ring instabilities, which were shown to be in good agreement with the predictions made by the Widnall instability (Robey et al. 2002).

Previous numerical studies have assumed that the initial clouds have a uniform density and sharp boundaries. However, real interstellar clouds have internal density gradients. For example, in molecular cloud cores with no embedded young stars, the density distributions are flat near the center and decrease with the distance from the cloud center (Bacmann et al. 2000). Observations of NGC 7293 (the Helix nebula) imply the presence of large radial density gradients in the cometary cloud cores there (Burkert & O’Dell 1998; O’Dell et al. 2000). The actual structure of the clouds is likely to be complex, but observations suggest that it would be worthwhile to study the effect of smooth density gradients on the cloud-shock interaction. Kornreich & Scalo (2000) have carried out the first such study. They derived an approximation for the distribution of vorticity generated in a shocked cloud with a smooth density profile. They argued that the vortex motions generated by the shock could be converted into turbulent motions observed in interstellar clouds provided that the motions are confined in the parent cloud. However, from their work, it was unclear whether such a cloud can survive after the shock passage. In fact, many numerical calculations have shown that uniform clouds, which have sharp density jumps at the cloud-intercloud boundaries, are easily destroyed primarily under the influence of Kelvin-Helmholtz and Rayleigh-Taylor instabilities (e.g., KMC). Recently, Poludnenko, Frank, & Blackman (2002) observed complete destruction for a cloud with a smooth but steep density gradient. It therefore remains an open question whether shocks can maintain turbulent motions in interstellar clouds.

In this paper, we study the effects of density gradients on the cloud destruction process, using our higher-order Godunov AMR hydrodynamic code (Truelove et al. 1998; Klein 1999). We first present two-dimensional axisymmetric calculations. A three-dimensional simulation is also done to clarify the property of turbulent motions generated by the shock-cloud interaction. In §2 we summarize the formulation of our problem. We show that at least 10^2 grids per cloud radius are needed to follow the evolution of smooth clouds accurately, just as in the uniform case. An overall description of shocked clouds is presented in §4, in which we demonstrate that the initial smooth density profile steepens after shock passage, and a density discontinuity is formed at the upstream side of the shocked cloud. A significant velocity shear develops across the discontinuity. The velocity shear makes this “slip surface” unstable to the Kelvin-Helmholtz instability, leading to complete cloud destruction even for smooth clouds. We also investigate the dependence of cloud evolution on the initial model parameters such as the density profile, shock strength, equation of state, and cloud shape. In §5, we estimate how the cloud is accelerated by the shock, which affects the growth rate of the Kelvin-Helmholtz instability, and therefore the timescale of cloud destruction. In §6 and §7, the formation of the slip surface and the subsequent cloud destruction are examined in more detail. Since the entire cloud is eventually destroyed by the shock, the vorticity generated by the shock is not confined to the original cloud. Instead, the shear motions are converted into random motions of small fragments after cloud fragmentation. In §8, the vorticity generated by shock passage is

compared with a simple analytic model. In §9, we summarize our results, and discuss how density gradients affect the observed morphologies of shocked clouds. We discuss several properties of turbulent motions generated by shock-cloud interaction, computing synthesized spectra and the velocity-size relation. Finally, we derive the condition under which shock waves are capable of triggering gravitational contraction of shocked clouds resulting in star formation.

2. Formulation of the Problem

2.1. A Cloud with a Smooth Boundary

In this paper, we investigate the hydrodynamic interaction of a planar shock with an interstellar cloud, focusing on the effect of a smooth cloud boundary. We consider a steady planar shock moving through the intercloud medium at a velocity v_b at infinity, corresponding to a Mach number $M \equiv v_b/C_{i0}$, where $C_{i0} = (\gamma_i P_{i0}/\rho_{i0})^{1/2}$ is the adiabatic sound speed in the intercloud medium. The subscript i denotes the values in the intercloud medium. The subscript 0 denotes the values in the preshock state. (In the following, the subscript 1 is used for the quantities in the post-shock state.) This shock hits a spherical cloud whose density distribution is given in a cylindrical coordinate system (ϖ, z) centered on the cloud by

$$\rho_0(\varpi, z) = \rho_{i0} + \frac{\rho_{c0} - \rho_{i0}}{1 + (r/r_{co})^n}, \quad (1)$$

where $r = (\varpi^2 + z^2)^{1/2}$, r_{co} is a characteristic radius, ρ_{c0} is the density at the cloud center, and ρ_{i0} is the density at infinity. The initial density contrast between the cloud center and the intercloud medium is

$$\chi \equiv \rho_{c0}/\rho_{i0}. \quad (2)$$

This density distribution is essentially the same as Kornreich & Scalo (2000), although they applied this profile to a cylindrical cloud with a two-dimensional Cartesian geometry. For comparison, we shall follow a couple of runs with Cartesian geometry. For $n \rightarrow \infty$, this model cloud reduces to a uniform cloud with a sharp boundary. Because we do not include the effect of gravity in our simulations, the cloud is assumed to be initially in pressure equilibrium with the ambient medium with a constant pressure P_0 everywhere in front of the shock. We also focus on nonradiative shocks, and therefore the ratio of specific heats is set to $\gamma = 5/3$ for most runs, although we calculate a couple of models with $\gamma = 1.1$ to examine the effects of radiative cooling.

In order to minimize the effects of the density variation along the initial shock front, we must begin our calculation with the shock in a region where the density variation is less than a few percent of the density at infinity (ρ_{i0}). Thus, the distance from the cloud center to the initial shock front is larger for clouds with smoother density gradients and/or larger density contrasts.

To measure the degree of mass concentration in the model cloud, we define two characteristic radii: a core radius, r_{co} , and a cloud radius, r_{cl} . The core radius denotes the size of the central

relatively flat region and is equal to the characteristic radius, r_{co} . The density at r_{co} is $(\chi^{-1} + 1)\rho_{\text{co}}/2$, which approaches $\rho_{\text{co}}/2$ for large χ . The cloud radius, r_{cl} , denotes the overall size of the cloud, and is defined to be the radius at which the density is twice that of the ambient medium ($2\rho_{i0}$),

$$r_{\text{cl}} = (\chi - 2)^{1/n} r_{\text{co}}. \quad (3)$$

We assume that $r_{\text{cl}} > r_{\text{co}}$, which is true for $\chi > 3$. These two characteristic radii divide the model cloud into two parts: the core ($r \leq r_{\text{co}}$) and the cloud envelope ($r_{\text{co}} < r \leq r_{\text{cl}}$). The region $r > r_{\text{cl}}$ is the intercloud medium. A third characteristic radius, the rms radius, is introduced in §2.3 below.

We define the core mass and the cloud mass in terms of density: The core mass, m_{co} , is the mass of gas with $\rho \geq 0.5(1 + \chi^{-1})\rho_{\text{co}}$, so that initially it is the mass inside r_{co} . The cloud mass is the mass with $\rho \geq 2\rho_{i1}$, so that initially it is the mass inside r_{cl} . These masses begin with values $m_{\text{co},0}$ and $m_{\text{cl},0}$, respectively, and then decrease due to shock heating and to mixing with the shocked intercloud medium. The degree of mass concentration in the initial cloud is measured by the ratio

$$\mathcal{R} \equiv \frac{m_{\text{cl},0}}{\frac{4}{3}\pi\rho_{\text{co}}r_{\text{co}}^3}, \quad (4)$$

which is unity for a uniform cloud, where $m_{\text{cl},0}$ is the initial cloud mass. In the following, the initial core mass, $m_{\text{co},0}$, is defined as the mass contained within $r \leq r_{\text{co}}$. For example, for $n = 2$ and large χ , we have $\mathcal{R} \rightarrow 4\chi^{1/2} - 3\pi/4$.

The thickness of the cloud boundary (h_{bd}) can be approximated as the density scale height at $r = r_{\text{co}}$,

$$h_{\text{bd}} = \left(\frac{\chi + 1}{\chi - 1}\right) \frac{2}{n} r_{\text{co}}. \quad (5)$$

In real interstellar clouds, the value of n is likely to vary widely. For example, in dense molecular cloud cores with no embedded young stars, the density profiles are flat near the center, follow a power-law profile of $\rho \propto r^{-2}$ in the intermediate radii, and fall steeply as $\rho \propto r^{-4}$ or even r^{-5} near the edges of the cores at $r \sim 10^4$ AU (Bacmann et al. 2000). Observations of the Helix nebula imply that the density distributions in the cloud cores can be fit with power-law profiles with $n \simeq 3 - 9$ (Burkert & O’Dell 1998; O’Dell et al. 2000). In the following, we vary n in the range of $2 \leq n \leq \infty$.

We do not take into account the effect of thermal conduction, which can play a role in evolution of non-magnetized clouds. According to KMC, non-magnetized clouds with $\chi \sim 10^2$ are ablated by evaporation in a time comparable to the cloud crushing time if the shocked intercloud medium is hot enough that the mean-free path is comparable to the cloud radius, so that the conduction is saturated (Cowie & McKee 1977). To neglect the effect of thermal conduction, we assume either that the intercloud medium is not that hot, or that there is a magnetic field that is too weak to be dynamically significant, but is strong enough to inhibit thermal conduction.

2.2. Time Scales

Following KMC, we define two characteristic time scales governing the evolution of the shocked cloud: (1) the shock-crossing time,

$$t_{\text{sc}} \equiv \frac{2r_{\text{co}}}{v_b}, \quad (6)$$

which is the time scale for the shock in the intercloud medium to sweep across the cloud, and (2) the cloud-crushing time,

$$t_{\text{cc}} \equiv \frac{\chi^{1/2} r_{\text{co}}}{v_b} = \frac{\chi^{1/2} r_{\text{co}}}{MC_{i0}} = \frac{r_{\text{co}}}{MC_{c0}} \quad (7)$$

$$= 0.98 \times 10^5 r_1 M_{10}^{-1} C_{c0,5}^{-1} \text{ yr} \quad (8)$$

where $r_1 \equiv r_{\text{co}}/1 \text{ pc}$, $M_{10} \equiv M/10$, $C_{c0,5} \equiv C_{c0}/10^5 \text{ cm s}^{-1}$, C_{c0} is the sound speed in the preshock cloud, C_{i0} is the sound speed in the preshock ISM, and t_{cc} is the time scale for the cloud to be crushed by the shock transmitted into the cloud. Here, the cloud-shock velocity is approximated as $v_s \simeq v_b/\chi^{1/2}$, since the pressure behind the cloud shock is comparable to that behind the intercloud shock for a strong shock ($\rho_{c0}v_s^2 \simeq \rho_{i0}v_b^2$, where v_s is the velocity of the cloud shock). We note that for smooth clouds, the actual mean velocity of the cloud shock is estimated as $v_s \simeq v_b/\langle\chi\rangle^{1/2}$, where the mean density contrast, $\langle\chi\rangle$, is generally smaller than χ . Therefore, for a smooth cloud, the cloud shock can reach the initial cloud center by the time of $1 t_{\text{cc}} \langle\chi\rangle/\chi (< 1 t_{\text{cc}})$.

According to McKee et al. (1987), the typical pressure variation timescale for a dense cloud in a Sedov-Taylor blast wave is given by $t_P \simeq 0.1 R_c/v_b$, where R_c is the distance from the origin of a blast wave. Therefore, our assumption of a steady shock requires that $t_{\text{cc}} \ll t_P$, or equivalently, that the cloud radius be smaller than $0.1 R_c/\chi^{1/2}$. This is known as the small cloud approximation (see §2 of KMC for more detail).

To investigate the overall evolution of the shocked clouds, we also define the following four characteristic timescales: (1) *the drag time*, t_{drag} , which is the time when the cloud velocity relative to the velocity of the post shock ambient flow has decreased by a factor of $1/e$ (see §5), (2) *the maximum expansion time*, t_m , which is the time when the effective cloud radius in the ϖ -direction (a) has increased to 90 % of its maximum value (see §5), (3) *the cloud destruction time*, t_{dest} , which is the time when the mass of the main axial fragment has become smaller than the initial cloud mass by a factor of $1/e$ (see §7), and (4) *the mixing time*, t_{mix} , which is the time when the mass of the region with $\rho \geq 2\rho_{i1}$ has reached half the initial cloud mass (see §7).

2.3. Global Quantities

Following KMC, we define several integrated physical quantities to study the cloud evolution. In KMC, a two-fluid treatment that followed both the cloud and intercloud matter allowed the global quantities to be evaluated by integrating the physical quantities only in the cloud material.

In this paper, we use a density threshold, ρ_{th} , to determine which material can be considered to be “cloud material.” The corresponding threshold mass is

$$m_{\text{th}} = \int_{\rho \geq \rho_{\text{th}}} \rho dV . \quad (9)$$

The threshold density ρ_{th} is chosen such that m_{th} corresponds to either the characteristic initial core mass ($m_{\text{co},0} \equiv m[r \leq r_{\text{co}}, t = 0]$) or the initial cloud mass ($m_{\text{cl},0}$). The regions with $m_{\text{co},0}$ and $m_{\text{cl},0}$ are then regarded as the core and cloud, respectively. The threshold densities ($\rho_{\text{th,core}}$ and $\rho_{\text{th,cl}}$) vary with time, and are obtained from eq. (9) by means of a bisection method. Unless noted otherwise, we will choose m_{cl} as the threshold mass to obtain the global quantities.

To measure the evolution of the cloud shape, we define the effective radii normal to and along the cylinder axis, a and c , respectively, as

$$a = \left(\frac{5}{2} \langle \varpi^2 \rangle \right)^{1/2}, \quad c = \left[5(\langle z^2 \rangle - \langle z \rangle^2) \right]^{1/2}, \quad (10)$$

where

$$\langle z \rangle = m_{\text{th}}^{-1} \int_{\rho \geq \rho_{\text{th}}} \rho z dV, \quad \langle z^2 \rangle = m_{\text{th}}^{-1} \int_{\rho \geq \rho_{\text{th}}} \rho z^2 dV, \quad (11)$$

$$\langle \varpi^2 \rangle = m_{\text{th}}^{-1} \int_{\rho \geq \rho_{\text{th}}} \rho \varpi^2 dV . \quad (12)$$

To measure the cloud destruction and turbulence, we define the velocity dispersions in the axial and radial directions, respectively, as

$$\delta v_z = (\langle v_z^2 \rangle - \langle v_z \rangle^2)^{1/2} \quad \text{and} \quad \delta v_\varpi = \langle v_\varpi^2 \rangle^{1/2}, \quad (13)$$

where

$$\langle v_z^2 \rangle = m_{\text{th}}^{-1} \int_{\rho \geq \rho_{\text{th}}} \rho v_z^2 dV, \quad \langle v_\varpi^2 \rangle = m_{\text{th}}^{-1} \int_{\rho \geq \rho_{\text{th}}} \rho v_\varpi^2 dV . \quad (14)$$

The mean velocity, $\langle v_z \rangle$, is defined as

$$\langle v_z \rangle = m_{\text{th}}^{-1} \int_{\rho \geq \rho_{\text{th}}} \rho v_z dV \quad (15)$$

where v_z is measured in the frame of the unshocked cloud. Finally, the mean density, $\langle \rho \rangle$, is defined as

$$\langle \rho \rangle = V_{\text{th}}^{-1} \int_{\rho \geq \rho_{\text{th}}} \rho dV, \quad (16)$$

where V_{th} is the volume of the region with $\rho \geq \rho_{\text{th}}$. In the following, the initial mean density is referred to as $\langle \rho_0 \rangle$ and the mean initial density contrast is defined as $\langle \chi \rangle = \langle \rho_0 \rangle / \rho_{i0}$.

3. Numerical Simulations

We solve the two-dimensional Euler equations of hydrodynamics using an Eulerian adaptive mesh refinement (AMR) hydrodynamic code with a second-order Godunov, dimensionally-split approach (Truelove et al. 1998; Klein 1999). In this code, as a computation proceeds and one wishes to resolve certain features within the flow, fine grids are dynamically created at locations meeting a pre-determined criterion, initialized from interpolated existing coarse grid data, and evolved. This entire process is continually repeated, allowing us to create and destroy fine grids in a general and controllable fashion, wherever and whenever the need arises (Truelove et al. 1998).

In this paper, the entire computational domain is covered with a base grid (level 1) and we use 2 additional levels of refinement (levels 2 and 3). The entire computation domain is covered with a base grid (level 1). Finer grids (levels 2 and 3) are created or destroyed by using two refinement criteria, a density criterion and density gradient criterion. The density criterion leads to refinement of cells in the base grid to level 2 when the density in these cells exceeds a threshold density, ρ_{ref} . In all the calculations presented in this paper, we set $\rho_{\text{ref}} = 1.2 \rho_{i1}$, where ρ_{i1} is the density of the post-shock ambient gas. This guarantees that the initial cloud ($\rho_0 \geq 2 \rho_{i0}$) is refined to at least level 2 after passage of the shock. We followed several models with different ρ_{ref} and found that the numerical results are essentially identical for $\rho_{\text{ref}} \lesssim 1.5 \rho_{i1}$ (i.e., the global quantities defined in the previous subsection are converged to within a few percent). The density gradient criterion leads to refinement of levels 1 or 2 when the local density scale height normalized by the cell size becomes smaller than a threshold value, \tilde{l}_{th} ,

$$\tilde{l}_j \equiv \frac{l_j}{\Delta x_j} = \frac{\rho_j}{(d\rho/dx|_j)\Delta x_j} < \tilde{l}_{\text{th}} , \quad (17)$$

where Δx_j denotes the grid spacing of the i -th grid and the density gradient $d\rho/dx|_j$ is computed at the cell center. We typically adopt $\tilde{l}_{\text{th}} = 20$ in this paper because the global quantities are converged to within a few percent for $\tilde{l}_{\text{th}} \geq 10$. This criterion guarantees that shock fronts and contact discontinuities are refined to level 2 in the region of $\rho < \rho_{\text{ref}}$ and to level 3 in the region of $\rho \geq \rho_{\text{ref}}$.

Our grids are Cartesian and properly nested; i.e., a fine grid must be surrounded by at least one layer of coarser cells. The only exception occurs at domain boundaries, where fine and coarse interfaces may coincide. The increase in resolution between levels, referred to as the refinement ratio, is taken to be 4 for every level.

The spatial resolution of the calculation is specified by the number of finest grid points that covers an initial core radius r_{co} . We use 120 finest grid points per core radius r_{co} as our standard resolution because we have demonstrated that with this resolution the evolution of the global quantities is well-converged. We refer to this resolution as R_{120} . More generally, we define the resolution of a calculation by R_N , where the subscript N is the number of cells per r_{co} at the finest level of refinement. The spatial resolutions we used in this paper and several characteristics of the initial clouds are summarized in Table 1.

Since our model cloud does not have a sharp boundary between the cloud and intercloud medium, we do not explicitly separate the cloud and intercloud medium as different fluids; i.e., we use a single-fluid version of the AMR code in which the ratio of the specific heats, γ , is always identical for both the cloud and intercloud medium. By contrast, KMC used a two-fluid code that treated the cloud and the intercloud medium as different fluids. When we approximate the effect of radiative losses by setting $\gamma \sim 1$, we must assume that both the cloud and the intercloud medium are radiative, whereas KMC were able to consider a radiative cloud in an adiabatic intercloud medium. As a result, our results for the radiative case differ from theirs (see §4.5).

3.1. Convergence Tests

In hydrodynamic simulations, it is very important to demonstrate that the calculations are performed at spatial resolutions that resolve important features of the hydrodynamic evolution such as the growth of hydrodynamic instabilities (see also KMC and Klein & Woods 1998). Comparing the time evolution of the global quantities at different spatial resolutions, KMC showed that at least 10^2 cells per cloud radius are needed to follow the interaction of shock waves with uniform clouds accurately. Here, we carry out a similar study for smooth clouds.

To perform the convergence study, we calculate two models for the shock-cloud interaction with $(n, \chi, M) = (2, 10, 10)$ and $(8, 10, 10)$ with different spatial resolutions ($R_{30}, R_{60}, R_{120}, R_{240}, R_{480}$, and R_{960} for $n = 8$ and $R_{30}, R_{60}, R_{120}, R_{240}$, and R_{480} for $n = 2$) and compare the global quantities. Figure 1 shows how the errors at the end of the calculation ($t = 3t_{cc}$ for $n = 8$ and $t = 6t_{cc}$ for $n = 2$) depend on the spatial resolution. The errors at a resolution R_N are defined as the differences between the global quantities at R_N and those at the finest resolution, R_f . In other words, for a global quantity Q_N measured at R_N , the error is

$$\Delta Q_N = \frac{|Q_N - Q_f|}{|Q_f|}. \quad (18)$$

The convergence test indicates that the errors of the velocity dispersions generally decrease in proportion to the inverse of the cell number N , which implies first-order accuracy. On the other hand, the convergence of the other quantities is better than that of the velocity dispersions; e.g., the errors in the radii a and c scale as N^{-2} . The slow convergence of the velocity dispersions may be related to the fact that the code accuracy is reduced to first order at discontinuities such as shocks and contact discontinuities, where substantial velocity differences are generated. All the quantities converge to within about 10 % for the spatial resolutions of R_{120} or finer. Hence, we conclude that at least $\sim 10^2$ cells per r_{co} are necessary for a converged calculation. In the following, we adopt R_{120} as the standard spatial resolution.

4. Numerical Results

In this section, we describe the overall evolution of clouds with smooth density profiles. In §4.1 and §4.2, we consider both clouds with a relatively steep density gradient ($n = 8$) and with a shallow density gradient ($n = 2$) as representative cases of nonradiative ($\gamma = 5/3$) clouds with smooth density profiles. In these models, the other parameters are fixed at a density contrast of $\chi = 10$ and a Mach number $M = 10$. The dependence of the results on the parameters n and χ is summarized in §4.3. In §4.4 we discuss the applicability of Mach scaling (see §4 of KMC) to smooth clouds. The effect of γ is studied in §4.5. Finally, the evolution of cylindrical clouds is compared with that of spherical clouds in §4.6.

In describing our results, we shall use r_{co} as a unit of length, ρ_{co} as a unit of density, and t_{cc} as a unit of time. Thus, our model is specified by four dimensionless parameters: n , χ , M , and γ . The evolution time is measured from the epoch at which the initial shock has reached to the point $z = -r_{co}$ on the z -axis. In Table 1, we summarize the parameters of the models presented in this paper.

According to previous studies, the overall evolution of shocked uniform clouds can be divided into four different stages: (1) the *initial transient stage*, in which an incident shock is transmitted into the cloud, and at the same time a bow shock or bow wave propagates into an upstream region; (2) the *shock compression stage*, in which the cloud is compressed mainly in the z -direction; (3) the *postshock expansion stage*, in which the shock-compressed cloud expands laterally, and (4) the *cloud destruction stage*, in which the shocked cloud is destroyed primarily by Kelvin-Helmholtz and Rayleigh-Taylor instabilities. As shown below, while the overall evolution of smooth clouds can also be divided into these four stages, there are significant differences in the morphology and evolution.

4.1. A Cloud With A Steep Density Gradient: AS8 ($n = 8$, $\chi = 10$, and $M = 10$)

To begin with, we consider a cloud with $n = 8$, $\chi = 10$, and $\gamma = 5/3$ interacting with a Mach 10 shock. In this model, about 70 % of the cloud mass is concentrated in the central core ($m_{co,0} \sim 0.7 m_{cl,0}$). There are several significant differences between the evolution of a uniform shocked cloud and a smooth shocked cloud, as we now describe.

In Figure 2, we present snapshots of the density distributions at seven different times. At the first encounter with the incident shock, the cloud is compressed mainly in the z -direction (the *initial transient stage*). In this stage, a shock reflects from the front of the cloud, propagating away from the cloud into the upstream postshock flow. The reflected shock develops into a bow shock, which can be recognized as a density jump in the upstream flow in Figures 2b and 2c. The bow shock eventually becomes a weak acoustic wave at later stages of evolution (Spitzer 1982). In fact, the bow shock is not so prominent in Fig. 2d as in Figures 2b and 2c. In Figure 2b, the shock passing

over the cloud envelope converges on the z -axis behind the cloud (at $z/r_{\text{co}} \simeq 1.5 - 2$ in Fig. 2b), reflects off the z -axis, and by a double Mach reflection drives a shock back into the shocked cloud. Thereafter, the shock transmitted into the front of the cloud (the cloud shock) interacts with the reflected shock after the cloud shock has passed through the high density region. (For the uniform case, this process occurs inside the cloud. Compare Fig. 2b and Fig. 2 of Klein et al. (1990).) This reflected shock compresses the shocked cloud from the rear in the z -direction (the *shock compression stage*). At this stage, the shocked cloud is deformed into an arc-like structure without any sign of the growth of instabilities (Fig. 2c). The cloud then expands laterally because the pressure is lower at the sides of the cloud compared to that on the axis (the *postshock expansion stage*, see also Nittman et al. (1982)). At the time shown in Figure 2d, the Kelvin-Helmholtz instability begins to develop along the slip surface, and eventually destroys the shocked cloud (the *cloud destruction stage*, see Figs. 2e, 2f, and 2g). The cloud has broken up into small fragments by the time shown in Figure 2f.

Since the velocity of the cloud shock is smaller in the higher density region (since $v \propto \rho^{-1/2}$), a significant velocity gradient develops in the cloud envelope. In the shock compression and postshock expansion stages, this velocity gradient in the cloud envelope steepens the initial smooth density profile at the front of the cloud, resulting in a sharp density jump (Fig. 2b). We refer to this density jump as a “*slip surface*” because the velocity is sheared parallel to its surface. The evolution of the slip surface is crucial in understanding the evolution of smooth clouds, because the growth rate of the Kelvin-Helmholtz instability across the surface depends on the thickness of the surface itself.

The convergence of the intercloud shock on the z -axis creates another strong reflected shock, which propagates downstream. It interacts with the intercloud shock to produce a Mach-reflected shock, which develops into a double Mach-reflected shock with two triple points. A powerful supersonic vortex ring forms just behind the Mach-reflected shock, and is carried away from the cloud with almost the same speed as the incident shock. The vortex ring propagates up to $(\varpi/r_{\text{co}}, z/r_{\text{co}}) \simeq (0.2, 5)$ in Figure 2c, and moves up to $(\varpi/r_{\text{co}}, z/r_{\text{co}}) \simeq (0.5, 11.4)$ and $(0.6, 17.6)$ in Figures. 2d and 2e, respectively.

Immediately after the shock passage, the morphology of the shocked cloud is significantly different from the uniform case, for which the lateral expansion occurs more rapidly and the Kelvin-Helmholtz instability starts to grow immediately after the shock passage. For example, for the uniform cloud, the ripple generated by the instability already appears along the cloud surface at $t \sim 1 t_{\text{cc}}$ [see Figs. 1- 4 of Klein et al. (1990)], and the arm-like structure starts to break up away from the cloud by $t \sim 3 t_{\text{cc}}$. For the smooth cloud, the cloud is deformed into an arch-like structure due to the shock compression, without any signs of the Kelvin-Helmholtz instability even at $2 t_{\text{cc}}$. The retarded growth of the instability is due to the fact that the instability grows faster for shorter wavelengths (the growth rate $\propto k^{-1}$, where k is the wavenumber), but is strongly suppressed for wavelengths shorter than the thickness of the shear layer [See Chapter 11 of Chandrasekhar (1961)]. *Therefore, cloud destruction is retarded until a density discontinuity develops; in this case, the density discontinuity is associated with the slip surface.* Also, the Richtmyer-Meshkov

instability, which grows linearly in time for small amplitudes, as opposed to the exponential growth of the Kelvin-Helmholtz and Rayleigh-Taylor instabilities in the linear regime, does not develop appreciably on the z -axis (Compare Fig. 2b and Fig. 5 of Klein et al. (1990)). In §6 and 7 we shall discuss in more detail the formation of the slip surface and the subsequent destruction of the cloud by the Kelvin-Helmholtz instability.

4.2. A Cloud With A Shallow Density Gradient: AS2 ($n = 2$, $\chi = 10$, and $M = 10$)

Next, we consider a very smooth cloud with $n = 2$. The other parameters are the same as those of the previous model: $\chi = 10$, $\gamma = 5/3$, and $M = 10$. The density profile of this cloud resembles that of a Bonner-Ebert sphere, or isothermal equilibrium sphere, which has a density profile $\rho \propto r^{-2}$ in its envelope. The cloud mass is less centrally concentrated than in the previous case ($m_{\text{co},0} = 0.10m_{\text{cl},0}$); only about 10 % of the total cloud mass is in the central core. Therefore, the smooth density profile has a greater effect for this model than for the $n = 8$ model presented in §4.1.

The shallow density gradient makes the interaction of the shock with the cloud milder than in the previous case. In Figure 3 we show snapshots of the density distributions of the shocked cloud. At the initial transient stage, a bow wave forms in the upstream flow, as can be seen at $z/r_{\text{co}} \simeq -2 \sim -1$ in Figs. 3b and 3c. However, it does not evolve into a shock, in contrast to the previous case and to the uniform cloud case. The reflected shock in the downstream flow is also weak. Because the effective density contrast between the cloud and intercloud medium is small ($\langle \rho_{\text{cl}} \rangle / \rho_{i0} \sim 2.9$) due to the small mass concentration, the mean relative velocity between the cloud and intercloud medium is also small. As a result, the intercloud shock does not converge on the z -axis at the rear of the cloud but instead interacts directly with the cloud shock (compare Figs. 2b and 3b). Thus, shock compression from the downstream side is weak, resulting in a slow lateral expansion. The interaction also produces a single Mach-reflected shock with a single triple point, which propagates away into the downstream flow from the cloud with almost the same speed as the intercloud shock (Figs. 3c, 3d, and 3e). Although the intercloud shock does not reflect from the z -axis, the postshock flow tends to converge on the z -axis, producing a vortex ring near the z -axis. This vortex ring propagates with a speed slower than the Mach reflected shock by a factor of ~ 0.75 .

Another effect of the shallow density gradient is a significant retardation in the formation of the slip surface. Because of the smaller mean relative velocity between the cloud and intercloud medium, it takes more time to form the slip surface. The Kelvin-Helmholtz instability grows very slowly due to both the small velocity shear and the retardation of the slip surface formation. An undulation along the slip surface does not appear until $t \sim 9t_{\text{cc}}$ (Fig. 3e), whereas in the $n = 8$ case, it already appears at $t \sim 4t_{\text{cc}}$ (Fig. 2d). Thus, it takes much more time for the cloud to be completely destroyed for $n = 2$ than for $n = 8$.

4.3. Dependence on n and χ

As mentioned in §2, our model is specified by four parameters: the power index of the density profile (n), the density contrast (χ), the strength of the incident shock (M), and the ratio of specific heats (γ). Here, we consider the effects of varying n and χ , which determine the mass distribution of the initial cloud. The dependence on M and γ will be discussed in subsequent subsections.

First, we consider the effect of the density gradient at the cloud boundary (see Figs. 2 and 3 and Tables 2 and 3). For smaller n , the interaction of the shock with the cloud is milder. For example, during the initial transient stage, the bow shock is weaker for smaller n , and the reflected shock and supersonic vortex ring formed at the downstream are less powerful. This is in part due to the fact that the mean relative velocity between the cloud and the intercloud medium decreases with n . For smaller n , the initial mean density contrast between the cloud and the intercloud medium ($\langle\chi\rangle = \langle\rho_{cl}\rangle/\rho_{i0}$) is smaller (see the seventh column of Table 1), and thus the relative velocity just after the initial shock passage is smaller, since

$$v_{\text{rel}} \equiv v_b - v_s \sim \left(1 - \langle\chi\rangle^{-1/2}\right) v_b \quad (19)$$

for strong shocks. This in turn delays the formation of the slip surface and therefore the onset of the Kelvin-Helmholtz and Rayleigh-Taylor instabilities. As a result, it takes longer for clouds with smaller n to be destroyed: The cloud destruction times t_{dest} for the $n = 2$ models are longer than for the $n = 8$ and $n = \infty$ models by factors of ~ 2 and ~ 3 , respectively (see §7 for the definition of t_{dest}).

The radial expansion is milder for smoother clouds; the radial expansion speed decreases with n because the relative velocity between the cloud and intercloud medium decreases with n (see §5.2). Also, the maximum effective radius normalized by the initial radius, a/a_0 , decreases monotonically with n , reflecting the fact that the shock-cloud interaction is milder for smaller n .

Next, we consider the effect of varying the density contrast χ . Figure 4 compares the snapshots of the $\chi = 100$ clouds with $n = 8$ and $n = 2$, and Table 3 summarizes the global quantities for $\chi = 100$ over a range of n . The most important effect of increasing the density contrast χ is that it leads to an increase in the relative velocity between the cloud and the intercloud medium (v_{rel} increases with $\langle\chi\rangle$ according to eq. 19 and $\langle\chi\rangle$ increases with χ according to Table 1). This leads to a longer drag time (see eq. [2.6] of KMC). More significantly, because the Kelvin-Helmholtz and Rayleigh-Taylor instabilities both depend on the relative velocity between the cloud and intercloud medium, (for the Rayleigh-Taylor instability, this is because the higher relative velocity leads to a greater acceleration) the higher relative velocities at higher χ lead to faster growth of the instabilities there. For example, for $n = 2$, a small-scale undulation of the slip surface due to the Kelvin-Helmholtz instability already appears at $t \sim 4 t_{\text{cc}}$ for $\chi = 100$, while it does not appear until $t \sim 8 t_{\text{cc}}$ for $\chi = 10$ (compare Figs. 4b and 3d). At $\chi = 100$, the Rayleigh-Taylor instability leads to substantial destruction of the cloud near the z -axis, whereas the Rayleigh-Taylor instability does not have significant effects at $\chi = 10$ (see Figs. 2 and 3). Our simulations also show that the

cloud destruction timescale measured in units of cloud-crushing times depends only weakly on χ . For the $\chi = 10$ and 100 clouds with the same values of n , the results for $t_{\text{dest}}/t_{\text{cc}}$ coincide within errors of ~ 10 percent (see Tables 2 and 3). This is consistent with the analytic estimate of KMC, which suggests that the growth times of the Kelvin-Helmholtz and Rayleigh-Taylor instabilities are comparable to the cloud-crushing time (see §2 of KMC).

Another important effect of increasing the density contrast is that the intercloud shock is able to converge onto the z -axis for very smooth clouds ($n = 2$) at $\chi = 100$, whereas it cannot do so at $\chi = 10$. As a result, at $\chi = 100$ a strong reverse shock is driven back into the cloud from the rear, compressing the cloud in the axial direction. After the reflected shock collides with the transmitted shock in the cloud, the cloud undergoes a steady expansion in the axial direction that increases with χ . At later times, the Rayleigh-Taylor instability also contributes to the larger effective radius in the axial direction. On the other hand, the radial expansion seems to reach an asymptotic value (see §5).

4.4. Dependence on M

4.4.1. Strong Shocks: Mach Scaling

For strong shocks ($M \rightarrow \infty$), the hydrodynamic equations for an inviscid gas are invariant under the transformation

$$t \rightarrow tM, \quad v \rightarrow v/M, \quad P \rightarrow P/M^2, \quad (20)$$

with the position and density unchanged. This is referred to as “Mach scaling”. For uniform clouds, KMC demonstrated that Mach scaling is reasonably valid. Here, we investigate whether Mach scaling is applicable to smooth clouds.

In Figure 5, we compare the density distributions of a cloud with $n = 8$, $\chi = 10$ and $\gamma = 5/3$ for two different Mach numbers, $M = 100$ and $M = 1000$. The clouds are depicted at two different times: $t = 3.5 t_{\text{cc}}$ (Figs. 5a and 5b) and $t = 6.4 t_{\text{cc}}$ (Figs. 5c and 5d). At the first epoch (Figs. 5a and 5b), the cloud morphologies are essentially the same. At the second epoch (Figs. 5c and 5d), morphological differences begin to appear at small scales, even though the overall morphologies remain similar. Those morphological differences become more significant at later stages. These deviations most likely originate from truncation errors and the artificial viscosity, which do not scale as equation (20).

In spite of the deviations in the cloud morphology, the global quantities agree very well even at late times if all the variables are scaled as in equation (20). For example, for the $M = 100$ and $M = 1000$ cases, the effective cloud radii and velocity dispersions coincide within about 5 percent and 10 percent, respectively, until the final stage of the computation ($t \sim 10 t_{\text{cc}}$). (Values of these quantities at $t = t_m \sim 5 t_{\text{cc}}$ are listed in Table 4.) The characteristic timescales such as t_{drag} , t_{dest} , t_{mix} , and t_m are in excellent agreement within errors of a few % for strong shocks.

4.4.2. Weak Shocks

Here we consider the weak shock case, in which Mach scaling is not applicable. We follow two cases with initial parameters that are the same as those of §4.1 and §4.2, except that the Mach number is $M = 1.5$.

In Table 4, we summarize the global quantities of the models with $(n, \chi, M) = (8, 10, 1.5)$ and $(2, 10, 1.5)$. Our numerical simulations show that the overall evolution of the weak shock case is qualitatively similar to that of the strong shock case. An important difference between the weak and strong shock cases is that cloud drag is less efficient in the weak-shock case, in part due to slower lateral expansion of the shocked cloud. For example, for $n = 8$ and 2, the drag times are $17.2 t_{cc}$ and $21.4 t_{cc}$, respectively, for the weak-shock case, whereas they are $3.3 t_{cc}$ and $7.5 t_{cc}$, respectively, for the strong-shock case.

Furthermore, the relative velocity between the cloud and intercloud medium is smaller in the weak-shock case, even after allowing for Mach scaling. This smaller relative velocity leads to slower growth of the Kelvin-Helmholtz instability (and thus slower cloud destruction). For example, for $n = 8$, the ripple along the slip surface due to the Kelvin-Helmholtz instability begins to appear at $t \sim 12 t_{cc}$ in the $M = 1.5$ case, while it already appears at $t \sim 4 t_{cc}$ for $M = 10$. Thus, the cloud destruction time is about 2 – 3 times longer in the weak-shock case.

The supersonic vortex ring is weak or absent for weak shocks. For $M = 1.5$ we did not observe the formation of a supersonic vortex ring for either $n = 8$ or $n = 2$, although the interaction between the reflected shock and the incident shock did generate a single triple point. Also, for the weak shock, a bow wave forms instead of a bow shock. Despite these qualitative differences between the strong and weak shock cases, the overall evolution of the weak shock case is quite similar to that of the strong shock case. We thus conclude that varying the strength of the incident shock does not alter our main conclusions on the shock-cloud interaction.

4.5. Dependence on γ : Effects of Radiative Losses

In the above subsections, we considered the evolution of nonradiative clouds, in which γ was set to $5/3$. Here, we consider the effects of radiative losses, which we model by setting $\gamma = 1.1$. Such a model is applicable for relatively large HI clouds and molecular clouds (e.g., KMC, Larson 2005) We recalculate the evolution of two models with $(n, \chi, M) = (8, 10, 10)$ and $(2, 10, 10)$. The numerical results are summarized in Table 5. Note that in our calculations, γ is 1.1 for both the cloud and the intercloud gas. In contrast, KMC set $\gamma = 5/3$ for the intercloud gas in their radiative calculations.

The softer equation of state leads to substantially greater compression; e.g., for the radiative model with $n = 8$, the effective radii, a and c , are reduced by as much as factors of 2.3 and 2.6, respectively, whereas for $\gamma = 5/3$, a and c are reduced by factors of 1.3 and 1.8, respectively. Thus,

the cross section of the radiative cloud is smaller than that of the nonradiative cloud, which lessens the efficiency of the cloud drag by the ambient flow. On the other hand, the post-shock intercloud density is higher than in the nonradiative case by a factor of about 4.7 (for $M = 10$). This higher intercloud density gives a greater drag force on the shocked cloud than in the nonradiative case (see eq. 21 below). In our calculations, the latter effect is more important, and as a result, the radiative drag times are much shorter than the nonradiative ones for both the $n = 8$ and $n = 2$ models. Because of this greater acceleration by the ambient gas, the relative velocity at the cloud boundary is rapidly reduced, leading to milder cloud destruction by the Kelvin-Helmholtz and Rayleigh-Taylor instabilities (see Table 5). The higher compression in the radiative case may facilitate gravitational collapse in the shocked cloud (§9).

4.6. Effect of Cloud Geometry

To investigate the effect of the cloud geometry, we consider cylindrical clouds. We adopt a Cartesian coordinate system (x, y, z) and assume that the physical quantities are uniform along the z -axis, which is identical to the cylinder axis. Mirror symmetry is assumed with respect to the x - z plane. The shock propagates in the y -direction. Hence, the x - and z -axes in this case correspond to the ϖ axis in the spherical case, and the y -axis in this case corresponds to the z -axis in the spherical case. In Table 6, we summarize the global quantities of the cylindrical clouds with $(n, \chi, M) = (2, 10, 10)$ and $(8, 10, 10)$. Comparison between the cylindrical and spherical clouds indicates that the cloud shape becomes more flattened and longer in the transverse direction for the cylindrical cloud. For example, for the $n = 8$ case, the effective radius in the transverse direction reaches $a/r_{\text{co}} \simeq 2.5$ in the cylindrical cloud, which is about 20 % larger than that of the spherical cloud with the same n . The somewhat greater expansion of the cylindrical cloud causes more efficient drag. Therefore, the cloud is accelerated more rapidly for the cylindrical cloud, leading to a slightly slower cloud destruction due to smaller relative velocities between the cloud and intercloud medium. This slower cloud destruction also causes a slower increase in the axial cloud size for the cylindrical cloud; at $t = 12 t_{\text{cc}}$, it reaches about $c/r_{\text{co}} \sim 4.0$ in the cylindrical cloud, while it reaches about $c/r_{\text{co}} \sim 4.7$ in the spherical cloud. In spite of these quantitative differences, the overall evolution of the cylindrical clouds is quite similar to that of the spherical clouds. Thus, we conclude that varying the cloud geometry does not alter our main conclusions obtained from the spherical calculations.

5. Cloud Drag

As shown above, the slip surface is subject to the Kelvin-Helmholtz and Rayleigh-Taylor instabilities, and as a result, the entire cloud is eventually destroyed. The acceleration of the cloud is responsible for the growth of the Rayleigh-Taylor instability, and the time history of the velocity, which is determined by the acceleration, governs the evolution of the Kelvin-Helmholtz instability. Therefore, it is very important to quantitatively understand the cloud acceleration. For uniform

clouds, KMC constructed a simple analytic formula for the cloud velocity that reproduced the numerical results quite well. Here, we extend their analytic model to smooth clouds.

5.1. Analytic Formula for the Cloud Velocity

According to §2 of KMC, the equation of motion for a shocked cloud can be expressed as

$$m_{\text{cl},0} \frac{dv_c}{dt} = -\frac{1}{2} C_D \rho_{i1} v_c^2 A(t) , \quad (21)$$

where $m_{\text{cl},0}$ is the cloud mass, v_c is the mean velocity of the cloud relative to the velocity of the shocked intercloud medium, ρ_{i1} is the density of the post-shock ambient medium, C_D is the cloud drag coefficient, and $A(t)$ is the time-dependent cross section of the cloud (see Figs. 2 and 3). As shown below in Figure 6, the cloud radius (a) is reduced slightly in the shock compression stage, and then increases significantly with time during the post-shock expansion stage. Thereafter, it does not change much after it reaches its maximum. Here, we approximate the evolution of the cross section of the cloud as

$$A(t) = \pi a^2 = \pi [a_0^2 + (C_c t)^2] \quad t \leq t_m \quad (22)$$

$$= \pi [a_0^2 + (C_c t_m)^2] \quad t > t_m , \quad (23)$$

where a_0 is the effective value of the initial cloud radius and C_c is the expansion velocity in the ϖ -direction. In this equation, we assume that the cloud expands at a constant speed, C_c , until it reaches its maximum transverse extent. We define the maximum expansion time, t_m , to be the time at which the effective radius in the ϖ -direction (a) has increased to 90 % of its maximum value. The maximum expansion times obtained from the numerical calculations are listed in Tables 2 – 6. Equation (23) is identical in form to the expression given by KMC, but there is an important difference: C_c is *not* necessarily equal to the sound speed in the cloud, but instead depends on model parameters.

In order to obtain a result that is directly comparable to that of KMC, we work in the frame of the shocked intercloud medium, denoted by a prime. Integrating equation (21) with respect to time, we obtain the following form of the cloud velocity,

$$\frac{v'_c}{v'_{c0}} = \left\{ 1 + \left(\frac{9C'_D}{8\chi^{1/2}} \right) \frac{t}{t_{cc}} \left[\frac{a_0^2}{r_{co}^2} + \frac{1}{3} \left(\frac{C_c}{v_s} \frac{t}{t_{cc}} \right)^2 \right] \right\}^{-1} \quad (t \leq t_m) \quad (24)$$

$$= \left\{ 1 + \left(\frac{9C'_D}{8\chi^{1/2}} \right) \left[\frac{a_0^2}{r_{co}^2} \frac{t}{t_{cc}} + \left(\frac{C_c}{v_s} \frac{t_m}{t_{cc}} \right)^2 \left(\frac{t}{t_{cc}} - \frac{2}{3} \frac{t_m}{t_{cc}} \right) \right] \right\}^{-1} \quad (t > t_m) \quad (25)$$

where

$$C'_D \equiv \frac{2}{3(\gamma_i - 1)\mathcal{R}} C_D. \quad (26)$$

We have assumed that the shock is strong ($M \gg 1$) and made the approximation $r_{\text{co}} \simeq v_s t_{\text{cc}}$, where $v_s \simeq v_b/\chi^{1/2}$ is the velocity of the transmitted cloud shock. This result is identical to that of KMC except that the drag coefficient C_D is replaced by an effective drag coefficient C'_D that can be much less than C_D for very smooth clouds (see below eq. 4). In the case considered by KMC (a uniform cloud [$\mathcal{R} = 1$] in an intercloud medium with $\gamma_i = \frac{5}{3}$), $C'_D = C_D$. The initial cloud velocity relative to the shocked ambient gas is $v'_{c0} = -2v_b/(\gamma + 1)$. In the following, we set the drag coefficient $C_D = 1$ (see KMC).

5.2. Comparison with Numerical Simulations

5.2.1. Cloud Shape

In the left panels of Fig. 6, we show the time evolution of the rms cloud radii, a and c . The cloud radius in the transverse direction, a , decreases with time in the shock compression stage, and then increases in the post-shock expansion stage, finally reaching a maximum. Thereafter, it shrinks by about 5%-30%, depending on n and χ , with the greater shrinkage occurring for the larger values of χ . On the other hand, the axial radius, c , keeps increasing with time. Thus, the shocked cloud becomes elongated in the direction of shock propagation. The initial reduction in the transverse radius due to shock compression happens at a later time for smaller n ; for $(\chi, M) = (10, 10)$, the radius a takes its minimum value at $t \sim 1.7 t_{\text{cc}}$ for $n = 8$ and $3.2 t_{\text{cc}}$ for $n = 2$. As n and χ increase, the cloud expands more rapidly, the aspect ratio of the shocked cloud, c/a , increases more rapidly, and the maximum value of a/a_0 increases.

For a uniform cloud, the expansion speed of the cloud can be approximated as the sound speed of the shocked cloud material (KMC),

$$\frac{C_c}{v_b} \simeq \frac{C_c}{\chi^{1/2} v_s} = \left[\frac{2\gamma(\gamma - 1)}{\chi(\gamma + 1)^2} \right]^{1/2}. \quad (27)$$

For $\chi = 10$, this gives $C_c = 0.56v_s$ for $\gamma = 5/3$. For smooth clouds, the expansion speeds are smaller: $C_c/v_s \sim 0.07, 0.23, \text{ and } 0.25$ for $n = 2, 4, \text{ and } 8$ with $\chi = 10$, respectively. The increase of expansion speed with n is due to the increase in relative velocity between the cloud and the intercloud medium as the cloud boundary becomes sharper and the mean density contrast larger; this in turn leads to a larger pressure difference between the shocked cloud and the intercloud medium.

The expansion speed also tends to increase with χ . In addition to the effect just described, the shock driven into the rear of the cloud augments the pressure in the cloud interior due to the transmitted shock. As a result, the radial expansion due to the pressure difference between the cloud and the side of the cloud is somewhat faster. Indeed, for $n \geq 8$ and $\chi \gg 10$, the expansion speed C_c is approximately equal to the adiabatic sound speed in the cloud, just as in the case of uniform clouds.

5.2.2. Cloud Velocity

In the right panels of Fig. 6, we compare the analytic result for the cloud velocity given in equation (25) with the value obtained from the numerical calculations. As shown in the figures, the expansion velocity C_c depends on n and χ . Since we determine C_c by fitting the evolution of the cloud radius a in the time interval $t \leq t_m$, our result for the cloud velocity is really only semi-analytic.

For clouds with a large density gradient, i.e., $n = 8$, our analytic model of the cloud velocity agrees well with the numerical results for both $\chi = 10$ and 100. For $\chi = 10$, the analytic cloud velocities are within about 25 % and 10 % of the numerical values for $t \leq t_{\text{drag}}$ and $t > t_{\text{drag}}$, respectively. The cloud velocity of the $n = 8$ cloud drops more slowly than the uniform case because its radial expansion is slower, and thus its cross section is smaller. For $\chi = 100$, the numerical values and analytic model agree to within 10 % until the radius a reaches its maximum. Thereafter, the deviation increases as the cloud undergoes a brief bout of acceleration, presumably due to the effects of the reverse shock. A similar effect is observed in some other models [see e.g., panel (d)], where it leads to a deviation from our model that is only temporary.

For smooth clouds with $n = 2$, the initial reduction in the effective cloud radius associated with the cloud compression significantly affects the cloud acceleration. Therefore, for such clouds we replace a_0 in eq. (23) with the time-averaged radius over the time interval $t_0 \leq t \leq t_1$, where t_0 is the time at which the shock first reaches the cloud surface on the z -axis, and t_1 is the time at which the cloud radius expands back to its initial value. This procedure reduces a_0 in eq. (23) by about 10% and 17% for $\chi = 10$ and 100, respectively. Even with this adjustment, the agreement between the analytic model and the numerical simulations at early times is not as good as for the $n = 8$ cases. This is because a significant fraction of the mass of the cloud is not much denser than the intercloud medium (the mean density contrast between the cloud and the intercloud medium is only $\langle \rho \rangle / \rho_{i0} \sim 3$ for the $n = 2$ case), and as a result the transmitted shock gives this gas a significant velocity. However, in deriving equation (25), we assumed that the cloud velocity is essentially zero immediately after the initial shock passage. At later times, the agreement between the analytic model and the numerical solution becomes much better in the $n = 2$ case: for $5 t_{cc} \lesssim t \lesssim 20 t_{cc}$, the agreement is within about 20 % for both $\chi = 10$ and 100. Note that the cloud was still expanding at the end of the calculation for $\chi = 100$ ($t < t_m$), so we were unable to fully test the model in this case.

In summary, our analytic model of the cloud drag can reproduce the numerical results reasonably well over a wide range of initial conditions.

6. Formation of the Slip Surface

As shown in §4, smooth clouds are completely destroyed by Kelvin-Helmholtz and Rayleigh-Taylor instabilities, whose growth rates depend on the wavelength of the perturbation. According to linear theory, the growth timescales of these instabilities are estimated as $t_{\text{KH}}/t_{\text{cc}} \sim v_b/(v_{\text{rel}}kr_{\text{co}})$ and $t_{\text{RT}}/t_{\text{cc}} = 1/(kr_{\text{co}})^{-1/2}$, respectively (see §2 of KMC), where k is the wavenumber of the perturbation. In both cases, the instability grows faster on smaller scales. Furthermore, linear theory shows that perturbations with wavelengths smaller than the thickness of the shear layer are stabilized significantly. Thus, the growth of the instabilities is closely related to the development of the slip surface. In this section, we investigate how a slip surface develops in a smooth cloud.

In Figures 7a – 7c, we represent the distributions of ρ , v_r , and v_z along $r = 0.5r_{\text{co}}$ at five different times for the cloud with small density gradient, i.e., $n = 8$ and $\chi = 10$. When the transmitted shock passes through the cloud (dash-dot-dot-dot curves), the maximum density increases by a factor of ~ 4 , as inferred from the jump condition, and then decreases as the cloud expands laterally. At the first encounter of the shock, the velocity shear layer is formed at the cloud envelope with a thickness h_{bd} . As can be seen in panel (c), the cloud envelope at the upstream side moves faster than the high density core, catching up with the high density core. As a result, the radial velocity profile becomes steep there [panel (b)], and thus the slip surface forms. At the same time, the density profile becomes steep and therefore the slip surface is also identical to a contact discontinuity. Here, we define the formation time of the slip surface, t_{slip} , as the time at which the radial velocity gradient reaches a first local maximum at the upstream side of the shocked cloud. In this model, t_{slip} is estimated as $t_{\text{slip}} \simeq 1.71 t_{\text{cc}}$. At $r = 0.5r_{\text{co}}$, where we measured the physical quantities, the slip surface is almost perpendicular to the z -axis, and thus the radial velocity difference across the slip surface can be regarded as the total velocity difference there. We note that the definition of t_{slip} depends on the position where the radial velocity is measured. However, as long as we measure the radial velocity gradient in the range of $0.3 \lesssim r/r_{\text{co}} \lesssim 0.7$, we get almost the same value. Thus, we measure t_{slip} at $r = 0.5r_{\text{co}}$ for all models. At $t \simeq 3t_{\text{cc}}$, the reverse shock compresses the cloud from the rear, and the cloud is squeezed from both sides by the reverse shock and the post-shock intercloud flow. Thus, the density gradient of the slip surface becomes very steep as can be seen in the solid curve in panel (a). The slip surface forms close to the core, and it can form only after the transmitted shock has reached the core.

For the cloud with small density gradient, i.e., $(n, \chi) = (2, 10)$, the shear layer has a wider thickness than for $n = 8$, at the first encounter of the shock. The lateral expansion of the core is a little faster for the smoother cloud, which leads to a smaller velocity difference between the core and intercloud medium. Because of this smaller velocity difference, the formation of the slip surface is retarded for the smooth cloud. In this model, t_{slip} is evaluated as $t_{\text{slip}} = 4.92 t_{\text{cc}}$. Since the reverse shock is weak in this model, the additional compression due to the reverse shock observed in the $n = 8$ case does not happen.

When the slip surface forms, the Kelvin-Helmholtz instability begins to develop and produce

ripples along it. For all the models calculated in this paper, the velocity dispersions in the axial and radial directions, δv_ϖ and δv_z , begin to rise at the epoch of ripple formation due to the Kelvin-Helmholtz instability. The time evolution of the velocity dispersions is shown in Figure 8 for two models with $(n, \chi, M) = (2, 10, 10)$ and $(8, 10, 10)$. For the $n = 8$ case, the velocity dispersions in the ϖ - and z -directions begin to increase at $t \simeq 2.3 t_{\text{cc}}$ and $3.2 t_{\text{cc}}$, respectively. For the $n = 2$ case, they begin to increase at $t \simeq 7 t_{\text{cc}}$ and $8 t_{\text{cc}}$, respectively. These times are in good agreement with the times of ripple formation ($3.5 t_{\text{cc}}$ and $8.4 t_{\text{cc}}$ for $n = 8$ and 2 , respectively). This indicates that the small-scale perturbations due to the Kelvin-Helmholtz instability indeed generate random motions of the small fragments. We note that the velocity dispersions in the axial and radial directions reach about 10 % of the incident shock velocity over a wide range of initial model parameters. They tend to be slightly larger for clouds with steeper density profiles (larger n — see Tables 2 through 6).

7. Cloud Destruction

The transmitted shock deforms a smooth cloud into an arc-like structure bounded by a slip surface. The slip surface is subject to the Kelvin-Helmholtz and Rayleigh-Taylor instabilities, which produce fragments that are swept away by the flow. Although their growth rates are smaller, fluctuations with larger wavelengths break the cloud into relatively large fragments, destroying the cloud more efficiently. On the other hand, fluctuations with smaller wavelengths contribute more efficiently to mixing the cloud material with the ambient gas. To evaluate these two processes of cloud destruction, we consider two different timescales: the cloud destruction time (t_{dest}) and the mixing time (t_{mix}), which are defined in §7.1 and §7.2, respectively.

7.1. Cloud Destruction Time: t_{dest}

When fluctuations with wavelengths comparable to the cloud size grow in time, they break the cloud into relatively large fragments. This large-scale fragmentation decreases the mass of the main body of the shocked cloud efficiently. To make a quantitative estimate of large-scale fragmentation, we follow KMC and define the cloud destruction time, t_{dest} , as the time at which the mass of the main axial fragment has become smaller than the initial cloud mass by a factor of $1/e$. The mass of the main axial fragment is evaluated as the mass of the gas that is physically connected to the main axial fragment by gas with $\rho > 2\rho_{i1}$. (Recall that the initial cloud is defined as the gas whose density is greater than $2\rho_{i0}$.) In practice, we identified the gas in the main axial fragment by drawing a density contour at a level of $2\rho_{i1}$ and then integrating the density in the region surrounded by the contour line.

In Tables 2 through 6, we summarize the cloud destruction times obtained from our numerical simulations. The cloud destruction time is longer for smoother clouds because both the Kelvin-Helmholtz and Rayleigh-Taylor instabilities grow more slowly in such clouds. For example, for

$n = 2$, $t_{\text{dest}}/t_{\text{cc}} \sim 10 - 12$, which is about three times larger than for the uniform case. On the other hand, $t_{\text{dest}}/t_{\text{cc}}$ depends only weakly on the initial density contrast, χ , because the growth rates of the Kelvin-Helmholtz and Rayleigh-Taylor instabilities scale with t_{cc} (see the previous section).

We note that our cloud destruction times of the uniform clouds tend to be smaller than those of KMC. For $\chi = 10$, we find $t_{\text{dest}} = 3.45 t_{\text{cc}}$ whereas they obtained $t_{\text{dest}} = 3.79 t_{\text{cc}}$; for $\chi = 100$, we find $t_{\text{dest}} = 3.02 t_{\text{cc}}$ vs. their value of $3.90 t_{\text{cc}}$. This is due to the fact that our cloud destruction time depends weakly on the threshold density of the main axial fragment, especially for large χ . In this paper, the threshold density of the main axial fragment is set to twice the shocked ambient density, $2\rho_{i1}$, for all the models. For smaller values of the threshold density, the cloud destruction time increases: For example, at $\chi = 100$, $t_{\text{dest}} \simeq 3.6 t_{\text{cc}}$ for $\rho_{\text{th}} = 1.5\rho_{i1}$, and $t_{\text{dest}} \simeq 3.86 t_{\text{cc}}$ for $\rho_{\text{th}} = 1.2\rho_{i1}$. Thus, our cloud destruction times seem to approach those of KMC as the threshold density decreases, and we expect them to coincide with those of KMC if we were able to count in all the cloud material.

7.2. Mixing Time: t_{mix}

Fluctuations with relatively short wavelengths, which have relatively large growth rates, are more effective at mixing cloud material with the the ambient gas than the long wavelength fluctuations that break up the cloud. To evaluate the efficiency of mixing, we define the mixing time, t_{mix} , as the time at which the mass of the region whose density is greater than $2\rho_{i1}$ (m_{cl}) reaches half the initial cloud mass ($m_{\text{cl},0}$).

In Figure 9, we depict the time evolution of the cloud mass normalized to its initial value, $m_{\text{cl}}/m_{\text{cl},0}$. The cloud mass decreases more rapidly for smooth clouds than for uniform clouds at early times, whereas at late times, it decreases more slowly. This indicates that the lower density gas in the cloud envelope tends to be mixed more rapidly, but the high density gas in the central core tends to be mixed only after the formation of the slip surface, which is a prerequisite for the onset of the Kelvin-Helmholtz instability and which is retarded for a smooth clouds. For the $n = 2$ models, the mixing time is determined by mixing of the envelope because of the large fractional mass of low density gas, whereas for models with larger n , the mixing time is determined by the KH instability.

Because the mixing time depends on relatively small-scale fluctuations, one might expect it to depend sensitively on the spatial resolution of the computation. However, comparison with different spatial resolutions [R_{30} , R_{60} , R_{120} , and R_{240} for $(n, \chi, M) = (8, 10, 10)$] shows that the mixing time at R_{120} is within 8 % of that at R_{240} , indicating that the mixing is reasonably accurate at R_{120} . Also, the errors of the mixing time decreases nearly in proportion to the inverse of the cell number, which implies first order accuracy.

Figure 10 shows how the cloud material is mixed with the ambient gas for two models:

$(n, \chi, M) = (8, 10, 10)$ and $(2, 10, 10)$. The histograms indicate the fraction of mass $\Delta m/m_{\text{cl},0}$ within a corresponding density bin with a width of $0.2\rho_{c0}$. For $n = 8$, about 50 % of the total cloud mass has density of $\simeq \rho_{c0}$ at the initial state. When the shock is transmitted into the cloud, the cloud density near the center increases by a factor of 4. At the same time, however, the shocked cloud starts lateral expansion, which reduces the density of the shocked cloud material. At $t \simeq t_{\text{cc}}$, the distribution of the mass fraction is roughly flat over the range $0.4\rho_{c0} \leq \rho \leq 4.4\rho_{c0}$. At this time, the cloud mass (the mass of gas with $\rho > 2\rho_{i1}$) has dropped to about 85% of the initial cloud mass. Gas from the initial cloud that is at lower densities corresponds to envelope gas that has been shocked by both an incident shock and a reverse shock. Two shocks increase the entropy of the shocked gas above that due to one shock. As a result the final density is only about twice the initial value (KMC), and some of the gas in the shocked envelope has a density below $2\rho_{i1}$. Mixing due to hydrodynamic instabilities starts at $t \sim 4t_{\text{cc}}$. As the cloud material mixes with the intercloud medium, the density of the mixed gas decreases with time, approaching the intercloud density with $\rho \simeq 0.4\rho_{c0}$.

At $t = 6.04t_{\text{cc}}$ (Fig. 10 c), the mass distribution has two peaks, at $\rho/\rho_{c0} \sim 0.7$ and 2.5. The higher-density peak at $\rho/\rho_{c0} \sim 2.5$ corresponds to the mass in the main axial fragment, which decreases with time. The lower-density peak at $\rho/\rho_{c0} \sim 0.7$ corresponds to the mass that is mixed by the shocked ambient medium. The low density peak shifts towards lower density with time, gradually approaching the density of the shocked ambient medium, $\rho_{i1} \sim 0.4\rho_{c0}$. By $t \simeq 10t_{\text{cc}}$, most of the cloud material has densities lower than $0.8\rho_{c0}$. On the other hand, for $n = 2$, most of the mass (about 80 % of the total mass) is already contained in the lowest density bin, $0.4\rho_{c0} \leq \Delta\rho < 0.6\rho_{c0}$. After passage of the shock, the density range of the cloud material widens immediately, although more than half the mass has a density less than ρ_{c0} . The Kelvin-Helmholtz instability mixes cloud material with the ambient medium, thereby reducing the mass fraction of the high density material. By the time shown in panel (h) of Fig. 10, most of the cloud material has a density $\sim 0.5\rho_{c0}$ owing to efficient mixing.

Our simulations demonstrate that the destruction and mixing of smooth clouds depend sensitively on the initial density distribution. In clouds with relatively steep density gradients, the core is almost completely destroyed by t_{mix} ; for example, for $n = 8$ and $\chi = 100$, the core mass is $0.10 m_0$ at $t = t_{\text{mix}}$ (recall that in this case, the core mass is the mass with $\rho > 0.51\rho_{c0}$). Thus, at this point the high density core is almost destroyed, and cloud mixing proceeds very efficiently throughout the entire cloud. By contrast, significantly more of the core survives for clouds with shallow density gradients: $m_{\text{co}}(t_{\text{mix}}) = 0.29m_{\text{co},0}$ for the model with $n = 4$ and $\chi = 100$, and $m_{\text{co}}(t_{\text{mix}}) = 0.25m_{\text{co},0}$ for the model with $n = 2$ and $\chi = 100$. For the case of a shallow density gradient, the cloud envelope is stripped from the main body of the cloud by $t = t_{\text{mix}}$, but much of the core remains intact. In such a core, the velocity dispersion is also relatively small, which indicates that random motions produced by the shock-cloud interaction are directly associated with cloud destruction, and do not significantly affect the cloud core before the core is destroyed.

8. Vorticity

The interaction of a shock wave with a cloud generates powerful vortex rings, which play an important role in the destruction of the cloud. For uniform clouds, KMC constructed a simple analytic model for vorticity production by the shock-cloud interaction that was in good agreement with their numerical results. In this section, we extend their model to the smooth clouds, and compare it with the numerical results presented in the previous sections.

8.1. Vorticity Production: Analytic Model

In the course of the shock-cloud interaction, vorticity is produced by the baroclinic term (the right-hand side of eq. [28]) in the vorticity equation for an inviscid fluid,

$$\frac{\partial \boldsymbol{\omega}}{\partial t} + \nabla \times (\boldsymbol{\omega} \times \mathbf{v}) = \nabla P \times \nabla \left(\frac{1}{\rho} \right). \quad (28)$$

Integrating the above equation over a cross section \mathbf{A} , we obtain the increase rate of circulation ($\Gamma \equiv \int \boldsymbol{\omega} \cdot d\mathbf{A}$),

$$\frac{d\Gamma}{dt} = \int \left(\nabla P \times \nabla \frac{1}{\rho} \right) \cdot d\mathbf{A}. \quad (29)$$

According to KMC, the vorticity production can be classified into four components. Two are associated with the cloud-intercloud boundary and are produced by the initial passage of the shock (Γ_{shock}) and by the subsequent post-shock flow (Γ_{post}). The third is associated with the triple points associated with the Mach reflected shocks behind the cloud (Γ_{ring}). The fourth is the vorticity produced in the cloud (Γ_{cloud}), which is smaller than those in the other components by a factor of order $\chi^{-1/2}$. As shown below, the vorticity production in smooth clouds is qualitatively similar to that in uniform clouds.

First, we consider the circulation produced by the initial passage of the shock, Γ_{shock} , defined as the circulation generated by the time at which the shock sweeps over the cloud and converges on the z -axis. For the uniform case, this component is generated only in a thin layer between the cloud and the intercloud medium. In contrast, for smooth clouds, the layer where this component is produced is extended in the radial direction because of the smooth cloud boundary. Indeed, as we shall see below, for smooth clouds such as those with $n = 2$ and $\chi = 10$, this circulation is produced throughout most of the cloud envelope, not just at the cloud surface. The time for the shock to sweep over the cloud is $t_{\text{sweep}} \sim 3a_0/v_b$. For uniform clouds, this estimate of the time scale coincides with that of KMC. KMC estimated the increase rate of Γ_{shock} as

$$\frac{d\Gamma}{dt} \simeq -\frac{3}{4} \left(\frac{v_b \cos \theta}{h} \right) \left(\frac{dz/\cos \theta}{dt} \right) h (1 - \chi^{-1/2}) = -\frac{3}{4} v_b^2 (1 - \chi^{-1/2}), \quad (30)$$

where θ is the angle at which the shock impacts the surface and h is the thickness of the shear layer, which is approximately the grid-cell size for uniform clouds. A strong shock is also assumed

(see eq. 7.8 of KMC for more details). KMC allowed for a reduction in the shear due to the motion of the shocked cloud by inserting a factor $(1 - \chi^{-1/2})$ in their final result for Γ_{shock} ; here we have included this factor in the original equation as well.

Equation (30) indicates that the rate of increase of Γ_{shock} is independent of the thickness of the shear layer. Thus, the fact that smooth clouds have a shear layer with a thickness $h \sim h_{\text{bd}}$, the scale height in the boundary (eq. 5), should not affect the growth of the circulation. Thus, we find

$$\Gamma_{\text{shock}} \simeq \frac{d\Gamma}{dt} \times t_{\text{sweep}} \simeq -\frac{9}{4}v_b a_0 (1 - \chi^{-1/2}) . \quad (31)$$

In the next subsection, we show that this simple model reproduces our numerical results reasonably well.

Next, we consider the vorticity production due to the interaction of the shocked cloud with the post-shock flow, Γ_{post} . When the initial shock passes through the cloud and the slip surface is formed at the upstream side of the cloud, the vorticity continues to be generated at the slip surface by the baroclinic term, which is non-zero when the density and pressure gradients are not parallel, and the equation of state is not barotropic. The pressure is approximately constant *across* the slip surface, but it varies *along* the slip surface, being a maximum at the stagnation point at the front of the cloud and smaller along the sides of the cloud. On the other hand, density varies primarily across the slip surface. Since the slip surface resembles the surface of the uniform cloud, we adopt KMC's equation for the growth of the post-shock circulation:

$$\frac{d\Gamma}{dt} \simeq \Delta P \Delta \left(\frac{1}{\rho} \right) \simeq -\frac{\Delta P}{\rho_{i1}} \simeq -\frac{1}{2}v_c'^2 . \quad (32)$$

Then, the circulation produced by the post-shock flow can be estimated as

$$\Gamma_{\text{post}} \simeq -\frac{1}{4}v_{c0}'^2 t_{\text{drag}} \simeq -\frac{9}{64} \left(\frac{\chi^{1/2} t_{\text{drag}}}{t_{\text{cc}}} \right) (1 - \chi^{-1/2})^2 v_b r_{\text{co}} , \quad (33)$$

where we have approximated the cloud velocity as $v_c' = v_{c0}' \exp(-t/t_{\text{drag}})$ with $v_{c0}' = [2v_b/(\gamma + 1)](1 - \chi^{-1/2})$. Here we have followed KMC in adopting a simpler approximation for the cloud velocity than that given in §2.3 (eqs. [24] and [25]).

Third, we consider the vorticity production associated with the triple points that are formed by the interaction of the initial shock and the reflected shock behind the cloud (Γ_{ring}). Following KMC, we estimate the circulation of the supersonic vortex ring as

$$\Gamma_{\text{ring}} = \frac{3}{4}v_b a_0 . \quad (34)$$

Note that this component has a positive sign, which is the opposite of Γ_{shock} and Γ_{post} (see §7.1 of KMC for more detail).

Finally, the vorticity produced in the core Γ_{core} , is expected to be smaller than Γ_{shock} and Γ_{post} by a factor of order $\chi^{-1/2}$. Since this is small, we follow KMC in not attempting to model this component.

Recently, Kornreich & Scalo (2000) constructed an analytic formula for the vorticity generated by the shock-cloud interaction for smooth clouds, which corresponds to our Γ_{shock} . They assumed that (1) the post-shock flow is steady and parallel to the z -axis, and (2) the velocity induced by the shock is inversely proportional to the square root of the pre-shock density. In order to make a comparison with our analytic model, we derive the circulation estimated from their model. From their eq. (40),

$$\begin{aligned} \Gamma_{\text{KS}} &= \int \boldsymbol{\omega} \cdot d\mathbf{A} = -\frac{2nr_{\text{co}}v_b}{\gamma+1}(1-M^{-2})(\chi-1) \\ &\times \int_0^\infty \frac{(r/r_{\text{co}})^n dr}{[(r/r_{\text{co}})^n + \chi]^{3/2}[1 + (r/r_{\text{co}})^n]^{1/2}}. \end{aligned} \quad (35)$$

We compare this to the numerical results below.

8.2. Comparison With Numerical Simulations

Figure 11, shows the time evolution of the total circulation, Γ , for several different models. For all the models, the evolution is qualitatively similar: Γ increases monotonically until the intercloud shock reaches the rear of the cloud, then decreases with time as the shock transmitted into the cloud interacts with the reflected shock on the z -axis. Thereafter, the total circulation increases again. The first peak corresponds to Γ_{shock} because at this time the incident shock has passed over the cloud and reached the z -axis at the rear of the cloud. The subsequent decrease in Γ corresponds to the positive contribution due to the supersonic vortex ring, Γ_{ring} . The interaction of the shocked cloud with the post-shock flow continues to generate the circulation Γ_{post} , so that the total circulation subsequently increases with time.

For clouds with relatively large density gradients [$(n, \chi) = (8, 10)$ and $(8, 100)$], the values of $\Gamma_{\text{shock}}/r_{\text{co}}v_b$ are predicted from eq. (31) as -1.77 and -2.58 , respectively, which are within about 15% and 30% of the peak values of the total circulation of -2.01 and -3.78 , respectively. Kornreich & Scalo (2000)'s model (see eq. 35) predicts $\Gamma_{\text{KS}} = -1.30$ and -2.18 for the two cases, which is somewhat less accurate than our model. Our numerical results show that the circulation associated with the supersonic vortex ring is about 1.02 for $(n, \chi) = (8, 10)$, which is close to our analytic estimate of 0.866. For $(n, \chi) = (8, 100)$, the numerical and analytic results are 1.40 and 0.953, respectively, again in good agreement. The analytic model predicts that the circulation due to the post-shock flow is $\Gamma_{\text{post}} \simeq -(0.48, 4.4)r_{\text{co}}v_b$ for the models with $\chi = 10$ and 100, respectively, which is in reasonable agreement with our final results. At the end of the computation, the total circulation is continuing to increase. However, we expect the rate of increase to decrease with time as the cloud becomes comoving with the post-shock flow so that the circulation will not increase much thereafter. Lower resolution calculations confirm this prediction.

The components of Γ_{post} and Γ_{ring} can be clearly seen in the spatial distribution of the circulation shown in Fig. 11, in which the vorticity is integrated from the bottom of the computation box

up to z , The cumulative circulation at $t = 2.86 t_{cc}$, shown in Fig. 12f, decreases with z , reaching a minimum value of $-2.3 r_{co} v_b$, which corresponds to Γ_{shock} . As z increases further, the circulation increases due to the contribution of the supersonic vortex ring, $\Gamma_{ring} = 1.0 r_{co} v_b$. For clouds with relatively steep density gradients (like $n = 8$), the spatial distribution of vorticity generated by the shock-cloud interaction is qualitatively similar to that of the uniform cloud (see Fig. 16 of KMC), i.e., immediately after the initial shock passage, the vorticity generated by the interaction is confined to a thin layer between the cloud and intercloud medium (Fig. 12b). In the subsequent evolution, the vorticity is concentrated in the slip surface, as can be seen in Fig. 12c.

For clouds with small density gradients, the analytic model continues to work well for the circulation produced by the shock. In this case, to estimate the circulation from the analytic model, we adopt the reduced initial cloud radii used in §5.2. For $(n, \chi) = (2, 10)$, our simulations show that the first peak in the circulation is $-3.10 r_{co} v_b$, compared with $\Gamma_{shock} = -3.41 r_{co} v_b$ from our analytic model. For $(n, \chi) = (2, 100)$ the corresponding values of the circulation are $-12.6 r_{co} v_b$ and $-14.1 r_{co} v_b$, respectively. Again, the analytic predictions are within about 12 % of our numerical results. In contrast, equation (34) overestimates the vorticity production by the supersonic vortex ring for the model with $n = 2$ and $\chi = 10$ by almost a factor 3 (our numerical results give $\Gamma_{ring} \simeq 0.591 r_{co} v_b$, whereas the analytic model predicts $\Gamma_{ring} = 1.66 r_{co} v_b$). In this model, the supersonic vortex ring is not as powerful as for the models with larger density gradients. As mentioned in §4.2, the vortex ring propagates more slowly than the triple point that moves with almost the same velocity as the incident shock v_b . This slower propagation speed of the supersonic vortex ring appears to be special to the $n=2$ and $\chi = 10$ model. For example, for the model with $n = 2$ and $\chi = 100$, a powerful supersonic vortex ring is formed after shock passage. The numerical result shows $\Gamma_{ring} \simeq 5.50 r_{co} v_b$, whereas the analytic solution predicts $\Gamma_{ring} = 5.25 r_{co} v_b$, about 5 % less than our numerical result.

For smooth clouds with $n = 2$, the analytic model of Kornreich & Scalo (2000) predicts $\Gamma_{KS}/r_{co} v_b = -3.98$ and -14.5 for $\chi = 10$ and 100, respectively. These values are in reasonable agreement with the numerical results given above, although once again the error is somewhat larger than for our analytic model.

For smooth clouds, the vorticity generated by the initial interaction with a shock extends throughout the cloud envelope (see Fig. 13b). However, this radially-extended vorticity shifts towards the slip surface with time. Eventually, the vorticity is concentrated in the slip surface, and is subsequently converted to random motions of small fragments as small-scale fragmentation proceeds.

We note that the evolution of the total circulation for the uniform clouds (*dotted curves* in Fig. 11) are apparently different from those of KMC (Figs. 13 and 15 of KMC) after the incident shock reaches the z -axis at the rear of the cloud. This discrepancy occurs because the contribution of the supersonic vortex ring is always included in our calculations, whereas KMC did not include it after the ring left the high-resolution part of the grid. If the contribution due to the supersonic

vortex ring is removed from our results, the evolution of the circulation is in good agreement with KMC’s results.

In summary, the analytic model constructed in §8 agrees well with our numerical results. Recently, Kornreich & Scalo (2000) claimed that the vorticity production in smooth clouds is not related to the baroclinic term, but is purely kinematic in origin; the preshock density distribution, which varies radially through the cloud, naturally generates the velocity gradient in the postshock cloud. However, the agreement between our theory and our simulations have clearly demonstrated that the vorticity is indeed produced by the baroclinic term in eq. (28) during the shock-cloud interaction. Their analytic model for vorticity production by the shock is somewhat less accurate than ours, since they did not consider the vorticity produced in the post-shock flow or in the supersonic vortex ring.

9. Discussion

9.1. Effect of a Smooth Cloud Boundary on Cloud Morphology: Implications for Observations

In this paper, we have studied the interaction of shocks with interstellar clouds with smooth density profiles. We showed that after several cloud crushing times, a slip surface with a significant density jump develops in front of the core of the shocked cloud, irrespective of the initial density distribution. Thus, the cloud is deformed into a head-tail structure before subsequent cloud destruction (see e.g., Figs. 2c and 3d). This suggests that the density profiles of observed shocked clouds should have significant density jumps in the direction of the source of the large scale shock. One might think that the effects of the initial density profile on cloud morphology would be obscured as the slip surface develops, but in fact information on the density profile remains imprinted on the shocked cloud until significant instabilities develop.

Figure 14 shows the time evolution of the ratio of the masses $m_{0.5}$ and $m_{0.1}$ for the models with $(n, \chi, M) = (2, 100, 10)$ and $(8, 100, 10)$, where $m_{0.5}$ and $m_{0.1}$ represent the masses contained within the regions with $\rho \geq 0.5 \rho_{\max}$ and $\rho \geq 0.1 \rho_{\max}$, respectively. Prior to cloud destruction, the mass ratio $m_{0.5}/m_{0.1}$ remains approximately constant, but varies significantly with n . For example, in the early stages of the shock-cloud interaction, the mass ratio stays at $m_{0.1}/m_{0.5} \gtrsim 0.5$ for clouds with relatively steep density gradients ($n \gtrsim 8$), whereas it is only about 0.1 for smooth clouds ($n \sim 2$). This suggests that observations of this mass ratio may be able to reveal the initial density profiles of the preshock clouds provided the clouds have not entered the shock destruction stage; the initial mass ratios \mathcal{R}^{-1} listed in Table 1 could be directly compared with the observed values.

Our simulations can be compared with the observations of young and middle-aged SNRs such as Cas-A and Cygnus Loop. Two important caveats in making any such comparison are that (1)

our simulations are non-magnetic, whereas magnetic fields are believed to be important in the interstellar medium, and (2) almost all of our simulations are adiabatic, whereas radiative losses are important in shocked interstellar gas. Recently, Patnaude et al. (2002) and Danforth et al. (2001) performed detailed investigation on the shock-cloud interactions observed in the Cygnus Loop (the XA and southwestern region of the Cygnus Loop). Their observations do not show any signs of the Kelvin-Helmholtz instability at the observed cloud surface, and thus they concluded that the interaction of the shock and cloud is in the initial transient stage. However, if the preshock cloud had a smooth density gradient at the cloud boundary, then the Kelvin-Helmholtz instability does not grow in the shock compression or the early post-shock expansion stages. If the mass ratio $m_{0.5}/m_{0.1}$ (or an equivalent one) could be estimated from the observations, then one might be able to infer something about the structure of the initial cloud.

9.2. Velocity Dispersions of Shocked Clouds

As shown above, the shock-cloud interaction produces vorticity inside the cloud. Much of the vorticity is concentrated at the slip surface, which is subject to the Kelvin-Helmholtz instability, and as a result the shocked cloud is distorted, producing vortex rings. Vortical motions generate substantial velocity dispersions. Recently, velocity dispersions generated by the shock-cloud interactions have attracted a great deal of attention as a mechanism for replenishing turbulent motions in the ISM (e.g., Kornreich & Scalo 2000; MacLow & Klessen 2003). Here, we discuss how velocity dispersions generated by shock passage evolve with time. First, we compute the synthesized spectra of turbulent motions integrated along the z -axis (see e.g., Falgarone et al. 1994), and then calculate the dependence of the velocity dispersion on region size, the so-called linewidth-size relation.

9.2.1. Synthesized Spectra of Shocked Clouds

Figures 15a through 15c show the evolution of the synthesized spectra of a shocked cloud with $(n, \chi, M) = (8, 10, 10)$. The synthesized spectra have been computed by averaging density-weighted histograms of the line-of-sight velocity over the entire cloud component. As mentioned in the next subsection, the velocity dispersions are typically subsonic for adiabatic shocks, and thus thermal broadening would smear the motions of small cloud fragments. Thus, to understand how the shocked cloud fragments due to hydrodynamic instabilities, we focus on the non-thermal motions. The line-of-sight is assumed to be parallel to the z -axis. At $t = 4 t_{cc}$, the synthesized spectrum has a fairly smooth profile with a peak at $0.6v_{i1}$, where v_{i1} is the velocity of the shocked intercloud medium, and a tail at higher velocities. At this stage, the cloud has not been destroyed, although it has been deformed into a head-tail structure (see Fig. 2d). The velocity component near the peak corresponds to the main body of the shocked cloud, while the higher velocity component corresponds to the tail of the shocked cloud. By $t = 8 t_{cc}$, the cloud has broken into small fragments, mainly due to the Kelvin-Helmholtz instability (see Fig. 2f). Each fragment has a different velocity,

which produces many spikes in the synthesized profile. The velocity dispersion of these fragments is estimated to be of the order of $0.1 v_b$, somewhat less than the sound speed behind the cloud shock ($\sim 0.18v_b$). The synthesized spectrum has a profile similar to panel (b) for $6t_{cc} \lesssim t \lesssim 10t_{cc}$. By $t = 13.2t_{cc}$ (Fig. 15 c), these spikes have become fainter and the peak velocity is shifting towards the post-shock ambient velocity as the cloud is accelerated and mixed with ambient medium by the interaction with the postshock flow. The component near the peak velocity has a velocity dispersion $\sim 0.05v_b$. The synthesized spectrum also has a plateau extending towards small velocities, which corresponds to the cloud components near the z -axis that were destroyed recently. This plateau becomes smaller with time.

Figures 15d through 15f show the evolution of the synthesized spectra for a shocked cloud with $(n, \chi, M) = (2, 10, 10)$. The overall evolution of these synthesized spectra is similar to that for the $n = 8$ case. Prior to the onset of the Kelvin-Helmholtz instability, the spectrum is more-or-less continuous and has a peak at low velocities, extending towards higher velocities. By $t = 12t_{cc}$, the cloud has begun to be destroyed and a number of spikes appear in the spectrum. The synthesized spectrum has a profile similar to panel (e) in the time interval of $10t_{cc} \lesssim t \lesssim 20t_{cc}$. At the late stage of cloud destruction, the peak of the spectrum shifts towards the velocity of the post-shock ambient medium. The evolution of the spectrum is slower than that of the $n = 8$ case because of the smaller relative velocity between the cloud and intercloud medium.

The dissipation of random motions seems to be slow compared to the cloud-crushing time. The velocity dispersion decreases by about 30 % from the maximum after $t = t_{\text{dest}}$ for $n = 8$, while for $n = 2$, the velocity dispersion does not decrease significantly after $t = t_{\text{dest}}$. On the other hand, for the uniform cloud (KMC), the velocity dispersion decreases by about 40 % by the end of computation ($10t_{cc}$). This reflects the fact that smoother clouds tend to evolve more slowly. The velocity dispersions would decrease more if further evolution is followed for smoother clouds. In the next subsection, we discuss how dissipation of random motions depend on the size, based on three-dimensional simulations.

9.2.2. *The Linewidth-Size Relation (3D simulation)*

Observations of the ISM indicate that interstellar clouds have nonthermal internal motions that are inferred to be supersonic turbulence. The observed velocity dispersions are found to scale with region size R as a power law, $\Delta v \sim R^p$, with $p = 0.4 - 0.6$ (e.g., Larson 1981; Myers 1987; Dame et al. 1986), although the power index p can depend on the environment (e.g., Caselli & Myers 1995). In this paper, we have shown that the interaction of shocks with interstellar clouds can generate random motions in the cloud material, but only by completely destroying the clouds. Here, we calculate the dependence of the velocity dispersion on region size, the so called linewidth-size relation, from our numerical results, and discuss whether random motions generated by the shock-cloud interaction agree with the observed scaling law. Because the characteristics of hydrodynamic turbulence depend strongly on the spatial dimension, we perform a three-dimensional calculation

with an intermediate spatial resolution R_{60} for the nonradiative cloud with $(n, \chi, M) = (8, 10, 10)$. We confirmed that all the global quantities in the three-dimensional calculation coincide with those of the two-dimensional calculation with the same spatial resolution to within 10% in the time interval $0 \leq t \leq 10 t_{cc}$.

In Fig. 16, we represent the linewidth-size relation for the model with $(n, M, \chi, \gamma) = (8, 10, 10, 5/3)$ at three different times: $t = 6 t_{cc}$, $8 t_{cc}$, and $10 t_{cc}$. The abscissa denotes the beam size, while the ordinate denotes the velocity dispersions of the cloud material. The figure shows the results of observing the shocked cloud from two different directions, (1) along the z -axis (perpendicular to the incident shock plane; shown by solid curves), and (2) perpendicular to the z -axis (in the plane of the incident shock; shown by dotted and dashed curves). In the latter case, we consider two different positions for the center of the observing beam: at the center of gravity, z_G , and downstream from that point, $z_G + r_{co}$, where the cloud is more disrupted than at $z = z_G$.

By $t = 6 t_{cc}$, the cloud has begun to experience significant destruction due to hydrodynamic instabilities, but at this stage the main axial core is still recognized on the z -axis (see Fig. 2). The solid and dotted curves have peaks at $\sim 0.3 r_{co}$ and $\sim 0.6 r_{co}$, respectively. These peaks correspond to the components near the main axial core. In the downstream observing beam, much of the cloud is mixed with the intercloud material, and the velocity dispersion (dashed curve) is almost independent of scale. This part of the cloud has been destroyed due to the nonlinear growth of small-scale Kelvin-Helmholtz instabilities. This indicates that the turbulent motions are generated mainly in the cloud envelope that has been destroyed, and in the cloud core, the turbulent generation delays. By $t = 8 t_{cc}$, the velocity dispersions in all the observing beams become relatively flat, indicating that the entire cloud is being destroyed due to the Kelvin-Helmholtz instabilities. Thereafter, the velocity dispersions in the small scale dissipate, as can be seen in Fig. 16(c). As a result of dissipation, at the time of $t = 10 t_{cc}$, if the velocity dispersions are approximated by power-laws as $\Delta v \sim R^p$, the power index is estimated as $p = 0.2 - 0.3$, although the power index depends on the direction and beam position. At later times, p increases somewhat since the small-scale fluctuations damp out more rapidly. Many numerical studies show that interstellar turbulent motions dissipate in a dynamical time, $L/\delta v$, where L is the size of the region (Elmegreen & Scalo 2004). At $t \simeq 8 t_{cc}$, we find $L/\delta v \simeq 0.53 t_{cc}$ and $2.9 t_{cc}$ at $L/r_{co} \approx 0.1$ and 1.0 , respectively, where we have averaged over three different beams. The velocity dispersion at small scales, $r \approx 0.1 r_{co}$, dissipates significantly from $t = 8 t_{cc}$ (Fig. 16b) to $t = 10 t_{cc}$ (Fig. 16c), whereas at large scales, $r \approx 1 r_{co}$, turbulent dissipation is less efficient. It appears that there has not been enough time to establish a self-consistent turbulent cascade to maintain the turbulent motions on small scales.

Our simulations show that at the early stage of cloud destruction, small-scale fluctuations dominate, which makes the linewidth-size relation flat. Subsequently, these small-scale fluctuations tend to damp out in a few cloud crushing times, leading to a linewidth that increases with scale. The linewidth-size relations obtained from our simulations are time-dependent and have not reached their asymptotic values. At late times, the cloud material dissolves into the ambient medium due to mixing, and therefore, it is difficult to distinguish them well. The turbulent cascade could also

influence the evolution of the linewidth-size relations, although our resolution is inadequate to study this precisely. Sytine et al. (2000) performed convergence tests on decaying turbulence with periodic boundary conditions and suggested that at least 1024^3 grids are needed to capture the characteristics of turbulent fields accurately. However, in our 3D simulation with R_{60} , the effective radius of the shocked cloud expands by a factor of two by $t = t_{\text{dest}}$, so that the shocked cloud is covered by only about 256^3 grids at the epoch of cloud destruction. Thus, to discuss the time evolution of the linewidth-size relation more accurately, higher resolution runs may be needed.

9.3. Implications for Interstellar Turbulence

The ISM is observed to be highly turbulent. Recently, Heiles & Troland (2003) found that the mass-weighted velocity dispersion is 7.1 km s^{-1} for cold neutral medium (CNM) clouds and 11.4 km s^{-1} for warm neutral medium (WNM) clouds. The one-dimensional rms Mach number of internal motions for individual CNM clouds is ~ 1.7 . The mean temperatures of the CNM and WNM are measured to be $\sim 70 \text{ K}$ and $\sim 8000 \text{ K}$, respectively. Under the assumption of pressure equilibrium between the CNM and the WNM, the typical density contrast between CNM and WNM clouds is of order $\chi = 100$. Heiles & Troland (2003) argue that the CNM clouds are organized into large sheets. More recently, Stanimirovic & Heiles (2005) have found very small CNM clouds, with column densities $\sim 10^{18} \text{ cm}^{-2}$. In this subsection, we discuss how our results on the shock-cloud interaction might be related to these observations.

Interstellar shocks are produced by several events such as supernova explosions and stellar winds from massive stars. Among them, the injection rate of energy into the ISM through supernovae is expected to exceed those of other sources (e.g., Castor 1993). Thus, we concentrate on the effects of supernova remnants (SNRs) and attempt to estimate the magnitude of the generated velocity dispersions. Most of the shock-cloud interactions are expected to be at low Mach numbers, because the shock speeds of SNRs rapidly decrease with expansion, although the typical Mach number is highly uncertain. In the following, we adopt the typical Mach number of $M \simeq 3$ as a representative value. For shocks at $M \simeq 3$, the distance from the origin of a blast wave R_c is estimated to be of the order of 100 pc (Cioffi, McKee & Bertschinger 1988). In this case, the small cloud approximation is applied for clouds with radii of the order of 1 pc or less. (see §2.2). This size is comparable to that of typical CNM clouds observed by Heiles & Troland (2003).

As shown above, the velocity dispersion induced by the shock-cloud interaction is of the order of

$$\delta v \simeq 0.074 v_b = 2.2 M_3 \chi_2^{1/2} C_{c0,5} \text{ km s}^{-1}, \quad (36)$$

for radiative clouds with $\gamma = 1.1$, where $M_3 \equiv M/3$, $\chi_2 \equiv \chi/10^2$, and $C_{c0,5} \equiv C_{c0}/10^5 \text{ cm s}^{-1}$. The above one-dimensional velocity dispersion $[\delta v^2 = (2\delta v_r^2 + \delta v_z^2)/3]$ is estimated as the mean value of the $n = 8$ and $n = 2$ clouds at $t = t_m$. For $T = 70 \text{ K}$, the one-dimensional velocity dispersion is computed as about 1.4 km s^{-1} . This magnitude of turbulence is comparable to the observed

internal velocity dispersions of CNM clouds, $\delta v \simeq 1.1 \text{ km s}^{-1}$, (Heiles & Troland 2003).

When one observes the ISM, it is difficult to directly distinguish the structures along the line-of-sight from observations. Approximating the thickness of the CNM to be $b = N_{\text{HI}}/n_{\text{HI}}$, Heiles & Troland (2003) infer that the CNM is in thin sheets with typical aspect ratios in the range of 100 – 300, where N_{HI} and n_{HI} are the column density along the line-of-sight and the volume density, respectively. If one observes a shocked cloud from the side and models it as a sheet of length $2c$, width $2a$, and thickness b , then the thickness b is evaluated as

$$b = \frac{N_{\text{HI}}}{n_{\text{HI}}} = \frac{m_{\text{cl},0}}{(2a \times 2c) \langle \rho_1 \rangle} = \frac{\pi a_0^3 M^2}{3ac}, \quad (37)$$

where we consider isothermal shocks. Then, the inferred aspect ratio is given by

$$2c/b = 6ac^2 M^2 / (\pi a_0^3). \quad (38)$$

For a shocked cloud, the above aspect ratio tends to be large and increases with time because the length c increases with time. For example, for a shocked cloud with $n = 8$, $\chi = 100$, and $M = 3$, the aspect ratio $2c/b$ reaches about 2000 at $t \simeq t_{\text{dest}}$. This implies that some of the observed CNM clouds with large aspect ratios could be shocked clouds torn up into small fragments, instead of thin sheets. Small cold clouds recently observed by Stanimirovic & Heiles (2005) could be related to this case. Since we don't take into account the magnetic fields, we cannot compare our result quantitatively with observations. The omission of the magnetic fields most likely leads to overestimation of the shocked density and therefore the aspect ratio. Although shocks in the real ISM are not isothermal as we assumed above, deviations from isothermality behind the shocks would cause only quantitative, not qualitative, changes in the result, provided that the cloud was initially CNM.

In our simulations, the vorticity generated by the shock-cloud interaction is converted into random motions of small cloud fragments produced by the Kelvin-Helmholtz and Rayleigh-Taylor instabilities. In that case, the CNM may consist of small shreds in a coherent flow. We note that this mechanism of turbulence generation is different from that of Kornreich & Scalo (2000), who proposed that the vorticity produced by the shock-cloud interaction is confined *inside the shocked cloud* and eventually converted into the turbulent motions observed in the interstellar clouds. They assumed that the smooth clouds are not destroyed significantly by shocks and that the density profile of the cloud is more or less maintained after shock passage. They suggest that the velocity dispersions generated by shock-cloud interaction can be scaled as $\Delta v/v_b = n^{1/2}(\rho_1 - \rho_0)/(2\rho_1)\chi^{-0.5} \propto \chi^{-0.5}$. However, our simulations have demonstrated that the density profile in the cloud changes significantly with time, and within a few cloud-crushing times a slip surface forms in front of the core of the cloud. In fact, the velocity dispersions are estimated as $\sim 0.1v_b$, which is more or less independent of χ . Furthermore, prior to complete cloud destruction, turbulent motions produced by the shock-cloud interaction are not induced in the cloud core, but in the cloud envelope. For example, for the model with $(n, \chi, M) = (2, 100, 10)$, the circulation in the cloud core (Γ_{co}), which has a density greater than $1.96 \rho_{\text{co}} [\approx 4 \rho_0(r = r_{\text{co}})]$ is $\Gamma_{\text{co}}/r_{\text{co}}v_b = 0.089$ at $t \simeq 1.5 t_{\text{cc}}$.

This value is only about 0.7 % of the total circulation ($\Gamma_{\text{tot}}/r_{\text{co}}v_b \sim 12$), indicating that most of the vorticity is in the cloud envelope. (If we use eq. 40 of Kornreich & Scalo (2000), which gives the distribution of vorticity as a function of radius, the circulation generated by the shock passage is estimated as $\Gamma_{\text{KS}}/r_{\text{co}}v_b = 0.039$ in the cloud core of $r \leq r_{\text{co}}$ and $\Gamma_{\text{KS}}/r_{\text{co}}v_b = 14.5$ in the whole region of $r \leq \infty$. These estimates from the KS theory also show that the shock-cloud interaction is ineffective at inducing turbulent motions in the cloud core.) For other models with larger n , the ratios of Γ_{co} to Γ_{tot} are much smaller than for $n = 2$.

In summary, the shock-cloud interaction can produce the magnitude of the velocity dispersions observed in the typical CNM clouds with the size of ~ 1 pc. However, turbulent motions produced by the shock-cloud interaction are directly associated with cloud destruction and, in the absence of a magnetic field at least, do not significantly affect the cloud core, contrary to Kornreich & Scalo (2000)’s view. The interaction of a shock with a cold H I cloud is expected to lead to the production of a spray of small H I shreds which have a coherent velocity distribution. Such structures could be related to the small cold clouds recently observed by Stanimirovic & Heiles (2005). However, we cannot make a realistic estimate for the size of the smallest shreds to compare with their observations, because our calculations do not include magnetic fields and thermal conduction (see e.g., Koyama & Inutsuka 2002 for the effect of thermal conduction).

9.4. Implications for Star Formation

Under some circumstances, compression due to interstellar shocks is expected to make a shocked cloud self-gravitating even if self-gravity is unimportant in the preshock cloud, thereby triggering star formation (Elmegreen & Lada 1977). Foster & Boss (1996) and Vanhala & Cameron (1998) numerically studied the interaction of radiative shocks with self-gravitating spherical clouds, showing that gravitational collapse can be induced by shock compression when radiative cooling is efficient in the shocked clouds. In particular, Foster & Boss (1996) studied the interaction of a critical Bonnor-Ebert sphere and a thin pulse-like wave that mimics an interstellar shock or wind, under the assumption that the gas is isothermal. They found a critical momentum of this wave above which gravitational collapse is induced after the interaction. Unfortunately, their result cannot be directly compared with ours because their initial conditions are different from ours; e.g., their initial wave is not satisfied with the shock jump condition. Vanhala & Cameron (1998) performed SPH simulations of the interaction of a planar shock and a spherical, centrally concentrated molecular cloud core, taking into account the effect of radiative cooling. They found that shocks with intermediate speeds of $20 - 45 \text{ km s}^{-1}$ are capable of triggering gravitational collapse since the effective γ of the shocked cloud remains close to unity. In contrast, stronger shocks inhibit gravitational collapse because the main coolants such as CO and H₂ are destroyed for velocities above about $40\text{-}50 \text{ km s}^{-1}$, driving the effective γ above $4/3$. This critical velocity for shock destruction of the molecules is consistent with that of Draine & McKee (1993). More recently, Hennebelle et al. (2003, 2004) studied the evolution of molecular cloud cores compressed by external pressure and

demonstrated that a compression wave triggers collapse from the outside in.

Here we first show that only radiative shocks can trigger gravitational instability in shocked clouds. We show that turbulence behind the shock has a strong stabilizing effect. Shocked clouds are compressed into a sheet-like configuration, and we analyze the condition for gravitational instability for this case following the treatment of Elmegreen & Elmegreen (1978). Since we have not included the effects of magnetic fields in our simulations, we neglect them here. Magnetic fields tend to stabilize against gravitational collapse, so the results below give necessary but not sufficient conditions for gravitational instability.

9.4.1. Maximum critical mass

Define the dimensionless cloud mass as (McKee & Holliman 1999)

$$\mu \equiv m_{\text{cl}} \left[\frac{(C_{cs}/\gamma_c^{1/2})^3}{(G^3 \rho_{cs})^{1/2}} \right]^{-1}, \quad (39)$$

where ρ_s and C_{cs} are the density and adiabatic sound speed at the surface of the cloud. A stable isothermal cloud has $\mu < 1.18$, the value for a Bonnor-Ebert sphere. More generally, a stable cloud has $\mu < \mu_{\text{cr}}$, where μ_{cr} is a number that, for polytropes ($P \propto \rho^{\gamma_p}$), depends on both the polytropic index γ_p and the adiabatic index γ (McKee & Holliman 1999). The maximum mass of a cloud in hydrostatic equilibrium (i.e., the cloud mass corresponding to μ_{cr} in eq. 39) is

$$m_{\text{cr}} \propto \left(\frac{P_s}{\rho_s^\gamma} \cdot \rho_s^{\gamma - \frac{4}{3}} \right)^{3/2}, \quad (40)$$

The first factor is proportional to the exponential of the entropy, and therefore always increases in shocks unless they are sub-isothermal (i.e., the post-shock temperature is less than the pre-shock temperature). Since the density also increases in shocks, we conclude that shocks increase the critical mass—i.e., they stabilize clouds against gravitational collapse—for $\gamma \geq \frac{4}{3}$. This is not surprising since clouds that are approximately locally adiabatic are stable against collapse for $\gamma > \frac{4}{3}$ in any case.

For $\gamma < \frac{4}{3}$, it is possible that the effect of the increased density might overcome the effect of the increased entropy in the expression for the critical mass. In fact, in the real ISM, radiative cooling can sometimes reduce the entropy of the postshock gas below the preshock value (a sub-isothermal shock). In that case, the above critical mass is likely to decrease below the preshock value, if turbulent motions generated by shock passage do not contribute to cloud support significantly.

In order to treat sub-isothermal shocks, we write the shock jump conditions as

$$\rho_1 v_1 = \rho_0 v_0, \quad (41)$$

$$\rho_1 (v_1^2 + \epsilon C_{\text{iso},0}^2) = \rho_0 (v_0^2 + C_{\text{iso},0}^2), \quad (42)$$

where $C_{\text{iso}} \equiv (P/\rho)^{1/2}$ is the isothermal sound speed and $\epsilon \equiv C_{\text{iso},1}^2/C_{\text{iso},0}^2$. Thus, $\epsilon = 1$ corresponds to an isothermal shock and $\epsilon < 1$ to a sub-isothermal shock; normal adiabatic shocks have $\epsilon > 1$. In shocked CNM clouds, the temperature might decrease to about 10 K if molecules can form behind the shock; in that case, $\epsilon \sim 0.1$. From the above relations, the post-shock density is

$$\rho_1 = \frac{M_{\text{iso}}^2}{\epsilon} F \rho_0, \quad (43)$$

where $M_{\text{iso}} \equiv v_0/C_{\text{iso},0}$ is the isothermal Mach number and

$$F = \left[\frac{1 + M_{\text{iso}}^{-2} + \sqrt{(1 + M_{\text{iso}}^{-2})^2 - 4\epsilon M_{\text{iso}}^{-2}}}{2} \right]. \quad (44)$$

The factor F approaches unity either for $\epsilon \rightarrow 1$ or for $M_{\text{iso}} \rightarrow \infty$ and $\epsilon/M_{\text{iso}}^2 \rightarrow 0$. In general, the factor F is about unity for $|1 - \epsilon|/M_{\text{iso}}^2 \ll 1$, which is true for sub-isothermal shocks provided the isothermal Mach number M_{iso} is not small; e.g., for $\epsilon = 0.1$ and $M_{\text{iso}} = 3$, $F \simeq 1.1$. Thus, the post-shock density can be approximated by $\rho_1 \simeq M_{\text{iso}}^2 \rho_0 / \epsilon$ for isothermal and sub-isothermal shocks.

We can obtain an upper bound on ϵ such that the shocked cloud is gravitationally unstable by assuming that the shocked cloud material is as localized as possible—i.e., it is spherical. Recall that μ is the ratio of the cloud mass to the critical mass (eq. 39), so that

$$\frac{\mu}{\mu_0} = \left(\frac{P_0^{3/2}}{\rho_0^2} \right) \left(\frac{\rho_1^2}{P_1^{3/2}} \right), \quad (45)$$

where μ_0 is the value of μ for the pre-shock cloud. Now, $P_1 \simeq M_{\text{iso}}^2 P_0$ and, for $F \simeq 1$, $\rho_1 \simeq (M_{\text{iso}}^2/\epsilon)\rho_0$ from equation (43). A necessary condition for gravitational instability is $\mu > \mu_{\text{cr}}$, which requires

$$\epsilon < (\mu_0 M_{\text{iso}} / \mu_{\text{cr}})^{1/2}. \quad (46)$$

Under the assumption that the pre-shock cloud is gravitationally stable, we have $\mu_0 < \mu_{\text{cr}}$, so the value of ϵ in this equation satisfies the condition that $F \simeq 1$ (i.e., $\epsilon/M_{\text{iso}}^2 \ll 1$) for $M_{\text{iso}} \gtrsim 3$. This equation suggests that arbitrarily strong radiative shocks can induce gravitational collapse, but two effects prevent this: non-thermal motions behind the shock (considered immediately below) and inadequate time for the gravitational instability to develop (considered in §9.4.2).

The shock-cloud interaction generates nonthermal motions behind the shock, both random and systematic, that tend to stabilize the cloud against gravitational collapse. In a radiative shock, these motions will dominate the thermal motions behind the shock so that equation (45) can be rewritten as

$$\frac{\mu}{\mu_0} \simeq \left(\frac{C_{c,\text{iso},0}}{\delta v_1} \right)^3 \left(\frac{\rho_1}{\rho_0} \right)^{1/2}. \quad (47)$$

Since δv_1 increases with scale, it must be evaluated on the same scale as μ/μ_0 . Our calculations are two-dimensional, so we estimate the one-dimensional velocity dispersion as $\delta v^2 = (2\delta v_r^2 + \delta v_z^2)/3$. Behind the shock, we express δv as a fraction of the shock velocity, $\delta v_1 = \kappa v_b \simeq \kappa \langle \chi \rangle^{1/2} v_0$, so that

$$\frac{\mu}{\mu_0} = \frac{F^{1/2}}{\kappa^3 \langle \chi \rangle^{3/2} M_{\text{iso}}^2 \epsilon^{1/2}}, \quad (48)$$

where we used equation (43) to evaluate the density jump. As remarked above, δv_1 and therefore κ increase with scale. When averaged over the entire shocked cloud, our numerical calculations give $\kappa \simeq 0.04 - 0.07$ for $t \simeq (1.5 - 2)t_{\text{cc}}$ for a uniform cloud with $\chi = 100$. Therefore, in typical CNM clouds, which have $\chi \sim 100$, the condition for instability ($\mu > \mu_{\text{cr}}$) restricts the Mach number to be

$$M_{\text{iso}} < \frac{F^{1/4} \mu_0^{1/2}}{\kappa_{-1}^{3/2} \langle \chi_2 \rangle^{3/4} \epsilon^{1/4} \mu_{\text{cr}}^{1/2}}, \quad (49)$$

where $\kappa_{-1} \equiv \kappa/0.1$ and $\chi_2 \equiv \chi/100$. For isothermal and sub-thermal shocks ($0 < \epsilon \leq 1$), we have $1 \leq F < 2$. We conclude that turbulence behind the shock stabilizes gravitational instability on the scale of the cloud for dense clouds ($\chi_2 \gtrsim 1$) unless the shock is relatively weak. Even for a very sub-thermal shock ($\epsilon = 0.1$ so that $F \simeq 2$) with $\kappa = 0.05$, instability is possible only if $M_{\text{iso}} < 6$. Magnetic fields, which we have not considered, also tend to stabilize the clouds against collapse.

9.4.2. Gravitational stability of a shocked layer

We turn now to a more detailed study of the gravitational instability of a shocked cloud, taking into account its geometry. The passage of a shock through a cloud that has an approximately uniform density (i.e., $n \gtrsim 4$) flattens it in the direction of shock propagation. The gravitational stability of a pressurized, isothermal sheet of gas was analyzed by Elmegreen & Elmegreen (1978). They showed that such a sheet is gravitationally unstable and fragments to form clumps, which may be filamentary. When the incident shock is very strong, the sheet is confined by a strong external pressure and exhibits effectively incompressible behavior. In this case, the most unstable mode has a wavelength that scales with the disk thickness and can be much shorter than the Jeans length (Elmegreen & Elmegreen 1978). Such a perturbation can have only a modest growth because the total mass is smaller than the critical Bonnor-Ebert mass. Only longer wavelengths, which grow more slowly, can contain more than a Bonnor-Ebert mass and lead to star formation. Three-dimensional numerical calculations by Umekawa (2002) showed that the stable clumps or filaments formed by the fastest growing modes can merge with themselves owing to mutual gravitational attraction, resulting in formation of more massive spherical cores (see also Umekawa et al. 1999); this is presumably equivalent to the growth of longer wavelength instabilities.

We assume that the mass of the pre-shock cloud is significantly less than the Bonnor-Ebert mass, so that it has approximately constant density—i.e., $n \rightarrow \infty$. Correspondingly, its temperature, and therefore sound speed, are approximately constant, both before and after the passage of

the shock. Elmegreen & Elmegreen (1978) analyzed the gravitational instability of an isothermal, planar layer of gas. They showed that the parameter that governs the properties of the instability is

$$A = \left(1 + \frac{P_1}{(\pi/2)G\Sigma_1^2}\right)^{-1/2}, \quad (50)$$

where Σ_1 is the surface density of the shocked sheet and P_1 is the pressure in the shocked intercloud medium and therefore at the surface of the shocked cloud.

The pressure in the midplane of the shocked cloud, P_{mid} , is greater than that at the surface, P_1 , due to self gravity: $P_1 = (1 - A^2)P_{\text{mid}}$ (Elmegreen & Elmegreen 1978). We now show that shocked clouds generally have $A \ll 1$, so that we can approximate the shocked sheet as isobaric. The surface density of the initial cloud, which is assumed to be uniform, is given in terms of μ_0 (the value of μ for the pre-shock cloud) by

$$\Sigma_0 = 0.83 \left(\frac{P_0}{G}\right)^{1/2} \mu_0^{1/3}. \quad (51)$$

The shock compresses the cloud in the transverse direction by a factor f (which is ~ 0.8 for $\gamma = 1.1$ and $\chi = 100$), so that $\Sigma_1 = f^{-2}\Sigma_0$. Approximating the pressure of the shocked cloud by $P_1 \simeq M^2P_0$, we then find that

$$\frac{P_1}{(\pi/2)G\Sigma_1^2} = 0.93 \frac{f^4 M^2}{\mu_0^{2/3}}. \quad (52)$$

For $M \gtrsim 3$ and $\mu_0 < 1$, this is large; as a result, the parameter A is small and the cloud is approximately isobaric.

Elmegreen & Elmegreen (1978) showed that not all unstable modes lead to gravitational collapse. For that to occur, two conditions must be satisfied: First, the mode must be large enough to capture a Bonnor-Ebert mass, which requires that the wavenumber k satisfies

$$kH < 0.91A^{1/2}(1 - A^2)^{1/4} \simeq 0.91A^{1/2}, \quad (53)$$

where $H = C_{c,1}(2\pi G\rho_{\text{mid}})^{-1/2}$ is the gravitational scale height of the shocked cloud. The corresponding e-folding time for the instability is

$$t_g \simeq (4\pi G\rho_{\text{mid}}kHA)^{-1/2}. \quad (54)$$

Second, the mode must grow fast enough that it becomes nonlinear during the age of the shock. Our results show that the density of the shocked cloud drops by a factor of 2 in $1.5 - 2t_{\text{cc}}$ for $10 \lesssim \chi \lesssim 100$, so we require that the growth time t_g be less than $2t_{\text{cc}}$. In units of the cloud-crushing time,

$$t_{\text{cc}} = \frac{r_{\text{co}}}{MC_{c0}} = 0.62 \frac{\mu_0^{1/3}}{M(G\rho_{c0})^{1/2}}, \quad (55)$$

the growth time of an unstable mode that encompasses at least a Bonnor-Ebert mass is then

$$\frac{t_g}{t_{cc}} = 0.47 f^{3/2} \left(\frac{\rho_{c0}}{\rho_{c1}} \right)^{1/2} \frac{M^{7/4}}{\mu_0^{7/12}}. \quad (56)$$

The condition for gravitational collapse to be possible is $t_g \lesssim 2t_{cc}$ as discussed above. Setting $F = 1$ in equation (43), this leads to

$$M \lesssim 7 \frac{\mu_0^{7/9}}{f^2 \epsilon^{2/3}}, \quad (57)$$

so that only shocks of moderate strength can initiate collapse. As discussed above, when the non-thermal motions behind the shock are taken into account, the maximum Mach number for collapse may be reduced further. The conclusion that shocked clouds are stable against collapse unless the Mach number is small differs from that of Vanhala & Cameron (1998) since they considered a cloud that is initially highly centrally concentrated, whereas we have assumed that the initial cloud is not self-gravitating and is therefore approximately uniform.

10. Conclusion

We have studied the interaction of shock waves with interstellar clouds, using a second-order, axisymmetric hydrodynamic code based on the Godunov method with local adaptive mesh refinement. This problem has been studied previously by KMC, who assumed that there is a discontinuous density jump between the cloud and the intercloud medium. In reality, one expects that the density distribution across the cloud boundary will be smooth due to thermal conduction, non-equilibrium cooling effects, or self-gravity (Kornreich & Scalo 2000). Here we have generalized the treatment of KMC to include the effects of smooth cloud boundaries on the shock-cloud interaction. We have considered a steady planar shock that strikes an initially spherical cloud with a density distribution that is flat near the center and decreases with radius as a power-law in the envelope. Our model can be specified by four numbers: n , the power-law index of the density distribution in the envelope; χ , the density contrast between the cloud center and the intercloud medium; M , the Mach number of the shock; and γ , the ratio of specific heats.

Our numerical simulations have shown that the clouds are completely destroyed, primarily by the Kelvin-Helmholtz instability, irrespective of the initial density distributions, although the smoothness of the initial density distribution affects the timescale of cloud destruction. For a cloud with $n = 2$ (the smoothest case we considered), the cloud destruction time is about 3 times longer than that of a uniform cloud. The timescale of the cloud destruction is closely related to the formation of a density discontinuity (the slip surface) at the upstream side of the shocked cloud. The slip surface is subject to the Kelvin-Helmholtz and Rayleigh-Taylor instabilities, and therefore significant cloud destruction starts there. Since the growth rates for these instabilities are larger for perturbations with shorter wavelengths in the linear regime and since the growth of perturbations

with wavelengths shorter than the thickness of the shear layer is greatly suppressed, the growth of the instabilities (and accordingly cloud destruction and mixing) are impeded prior to the formation of the slip surface. It therefore takes more time for shocks to destroy clouds with smoother density gradients.

We have constructed simple analytic models describing the time evolution of the cloud velocity and the circulation that agree well with our numerical results. The vorticity is produced by the baroclinic term in the vorticity equation, and can be divided into four components: (1) Γ_{shock} , which is generated by the initial shock-cloud interaction, (2) Γ_{post} , which is continuously produced by the interaction between the shocked cloud and post-shock intercloud flow, (3) Γ_{ring} , which is produced in the intercloud region by the supersonic vortex ring, and (4) Γ_{cloud} , which is the circulation produced in the cloud and is smaller than other components by a factor of $\chi^{-1/2}$. For smooth clouds with $n = 2$, the first component is generated throughout the cloud envelope after the initial shock passage, as discussed by Kornreich & Scalo (2000). However, most of the vorticity generated inside the cloud shifts towards the upstream side of the cloud, being concentrated in the slip surface, and eventually is converted into random motions of small fragments that are detached from the main cloud.

Vortical motions due to hydrodynamic instabilities produce substantial velocity dispersions in the shocked cloud. The vortical motions generated in the cloud are converted into random motions of small fragments shredded from the parent clouds. Over the wide range of initial model parameters considered here, the one-dimensional velocity dispersions are typically $\delta v \sim 0.1v_b$, which is estimated as about 2 km s^{-1} for $T \simeq 70 \text{ K}$, $\chi \simeq 10^2$, and $M \simeq 3$. Such velocity dispersions are consistent with the observed internal motions of about 1.5 km s^{-1} in the CNM (Heiles & Troland 2003). Recently, Heiles & Troland (2003) suggest that the CNM is in thin sheets with large aspect ratios, by assuming that the thickness along the line-of-sight is estimated to be $b = N_{\text{HI}}/n_{\text{HI}}$. If we apply the same procedure to estimate the aspect ratios, then the shocked clouds torn up into small fragments also have large aspect ratios, and therefore, some of the observed CNM clouds could be explained by the shocked clouds, instead of thin sheets.

At the early stage of cloud destruction, the small-scale fluctuations are dominant due to the nonlinear growth of the Kelvin-Helmholtz instability. Thus, the linewidth-size relation in a shocked cloud is expected to be relatively flat. Thereafter, the small-scale fluctuations tend to damp gradually with time, leading to a linewidth that increases with size.

Under some circumstances, shock compression may induce gravitational collapse, leading to triggered star formation. We have discussed how the critical Bonnor-Ebert mass changes due to shock passage. The critical Bonnor-Ebert mass can decrease only when $\gamma < 4/3$. Radiative shocks are often assumed to be isothermal, but in fact they are generally sub-isothermal. We have determined the density jump across a sub-isothermal shock and shown that, in the absence of significant nonthermal motions behind the shock, star formation can be induced in an initially uniform cloud by a shock only if it is of moderate strength. Our results indicate that the postshock

gas has significant nonthermal motions, and this can further limit the onset of gravitational collapse.

We would like to thank M. R. Krumholz for making his valuable IDL codes available to us and for stimulating discussion on interstellar turbulence. We also thank R. K. Crockett, D. Gies, and J. Walters for a number of valuable conversations. F. N. acknowledges the support of the JSPS Postdoctoral Fellowship for Research Abroad. He is also grateful to the Astronomy Department, University of California at Berkeley for the kind hospitality during his stay. CFM gratefully acknowledges the support of the Miller Institute for Basic Research and of the NSF through grant AST-0098365. Part of this work was supported by NASA ATP grant NAG5-12042 (RIK and CFM) and under the auspices of the US Department of Energy at the Lawrence Livermore National laboratory under contract W-7405-Eng-48 (RIK and RTF). Computations were made possible by the NSF San Diego Supercomputer Center through NPACI program grant UCB267 (RIK et al.).

REFERENCES

- Bacmann, A., André, P., Puget, J.-L., Abergel, A. Bontemps, S., Ward-Thompson, D. 2000, *A&A*, 361, 555
- Bedogni, R. & Woodward, R. R., 1990, *A&A*, 231, 481
- Burkert, A. & O’Dell, C. R. 1998, *ApJ*, 503, 792
- Caselli, P. & Myers, P. C. 1995, *ApJ*, 446, 665
- Castor, J. I. 1993, in *ASP Conf. Ser. 35, Massive Stars: Their Lives in the Interstellar Medium*, ed. J. P. Cassinelli & E.B. Churchwell (San Francisco:ASP), p. 297
- Chandrasekhar, S. 1961, *Hydrodynamic and Hydromagnetic Stability* (New York:Dover)
- Cioffi, D. F., McKee, C. F., & Bertschinger, E., 1988, *ApJ*, 334, 252
- Cox, D. P. & Smith, B. W., 1974, *ApJ*, 189, L105
- Cowie, L. L. & McKee, C. F., 1977, *ApJ*, 211, 135
- Dai, W., & Woodward, P.R. 1994, *ApJ*, 436, 776
- Dame, T. M., Elmegreen, B. G., Cohen, R. S. & Thaddeus, P. 1986, *ApJ*, 305, 892
- Danforth, C. W., Blair, W. P., & Raymond, J. C. 2001, *AJ*, 122, 938
- Draine, B. T. & McKee, C. F. 1993, *ARA&A*, 31, 373
- Elmegreen, B. G., & Elmegreen, D. B. 1978, *ApJ*, 220, 1051

- Elmegreen, B. G., & Lada, C. J., 1977, *ApJ*, 214, 725
- Elmegreen, B. G., & Scalo, J., 2004, *ARA&A*, 42, 211
- Falgarone, E., Lis, D. C., Phillips, T. G., Pouquet, A., Porter, D. H., & Woodward, P. R. 1994, *ApJ*, 436, 728
- Foster, P. N. & Boss, A. P. 1996, *ApJ*, 468, 784
- Gregori, G., Miniati, F., Ryu, D. & Jones T.W. 2000, *ApJ*, 543, 775
- Heathcote, S. R. & Brand, P. W. 1983, *MNRAS*, 203, 67
- Heiles, C. & Troland, T. H. 2003, *ApJ*, 586, 1067
- Hennebelle, P., Whitworth, A. P., Goodwin, S. P., & Andre, P. *MNRAS*, 340, 870
- Hennebelle, P., Whitworth, A. P., Cha, S.-H., & Goodwin, S. P. *MNRAS*, 348, 687
- Klein, R. I. 1999, *Jour. Comp. Appl. Math.* 109, 123
- Klein, R. I., McKee, C. F., & Colella, P. 1990, in *The Evolution of the Interstellar Medium*, ed. L. Blitz (San Francisco:ASP), p.117
- Klein, R. I., McKee, C. F., & Colella, P. 1994, *ApJ*, 420, 213
- Klein, R. I. & McKee, C. F. 1994, in *Numerical Simulations in Astrophysics: Modeling the Dynamics of the Universe*, eds. J. Franco, S. Lizano, L. Aquilar, and E.Daltabuit (Cambridge University Press), p. 251
- Klein, R. I. & Wood, D. T. 1998, *ApJ*, 497, 777
- Klein, R. I., Budil, K. S., Perry, T. S., & Bach, D. R. 2000, *ApJS*, 127, 379
- Klein, R. I., Budil, K. S., Perry, T. S., & Bach, D. R. 2003, *ApJ*, 583, 245
- Kornreich, P. & Scalo, J. 2000, *ApJ*, 531, 366
- Koyama, H. & Inutsuka, S. 2002, *ApJ*, 564, L97
- Landau, L. D., & Lifshitz, E. M. 1959, *Fluid Mechanics* (Reading: Addison-Wesley)
- Larson, R. B. 1981, *MNRAS*, 194, 809
- Larson, R. B. 1985, *MNRAS*, 214, 379
- Larson, R. B. 2005, *MNRAS*, 359, 211
- Mac Low, M.-M., McKee, C. F., Klein, R. I., Stone, J. M., & Norman, M. L. 1994, *ApJ*, 433, 757

- Mac Low, M.-M. & Klessen, R. 2004, *Rev. Mod. Phys.*, 76, 125
- McKee, C. F. & Cowie, L. L. 1975, *ApJ*, 195, 715
- McKee, C. F., Hollenbach, D. J., Seab, C. G., & Tielens, A. 1987, *ApJ*, 318, 674
- McKee, C. F. & Holliman II, J. H. 1999, *ApJ*, 522, 313
- McKee, C. F. & Ostriker, J. P. 1977, *ApJ*, 218, 148
- Myers, P. C. in *Interstellar Processes*, ed. D.J. Hollenbach & H. A. Thronson (D. Reidel Publishing Company, Dordrecht), p.71
- Nittman, J., Falle, S., & Gaskell, P. 1982, *MNRAS*, 201, 833
- Nulsen, P. E. J. 1982, *MNRAS*, 198, 1007
- O'Dell, C. R., Henney, W. J., & Burkert, A. 2000, *AJ*, 119, 2910
- Patnaude, D. J., Fesen, R. A., Raymond, J. C., Levenson, N. A., Graham, J. R., & Wallace, D. J. 2002, *AJ*, 124, 2118
- Poludnenko, A. Y., Frank, A., & Blackman, E.G. 2002, *ApJ*, 576, 832
- Robey, H. F., Perry, T. S., Klein, R. I., Kane, J. O., Greenough, J. A., & Boehly, T. R. 2002, *Phys. Rev. Lett.*, 89, 5001
- Ryutov, D., Drake, R. P., Kane, J., Liang, E., Remington, B. A., & Wood-Vasey, W. M. 1999, *ApJ*, 518, 821
- Schiano, A.V.R., Christiansen, W.A., & Knerr, J.M. 1995, *ApJ*, 439, 237
- Sgro, A. G. 1975, *ApJ*, 197, 621
- Spitzer, L. 1982, *ApJ*, 262, 315
- Stanimirovic, S., & Heiles, C. 2005, *astro-ph/0505106*
- Stone, J. M. & Norman, M. L. 1992, *ApJ*, 390, L17
- Sytine, I. V., Porter, D. H., Woodward, P. R., Hodson, S. W., & Winkler, K.-H. 2000, *Jour. Comp. Phys.*, 158, 225
- Tenorio-Tagle, G. & Rozyczka, M. 1986, *A&A*, 155, 120
- Truelove, J. K., Klein, R. I., McKee, C. F., Holloman II, J. H., Howell, L. H., Greenough, J. A., & Woods, D. T. 1998, *ApJ*, 495, 821
- Umekawa, M., Matsumoto, R., Miyaji, S., & Yoshida, T. 1999, *PASJ*, 51, 625

- Umekawa, M. 2002, in The Proceedings of the IAU 8th Asian-Pacific Regional Meeting, Volume II. eds. S. Ikeuchi, J. Hearnshaw, and T. Hanawa, (the Astronomical Society of Japan) p. 227
- Vanhala, H. A. T. & Cameron, A. G. W. 1998, ApJ, 508, 291
- Vazquez-Semadeni, E., Ostriker, E. C., Passot, T., Gammie, C. F., & Stone, J. M. 2000, in Protostar and Planets IV, eds. V. Mannings, Boss, A. P., & Russell, S. S. (The University of Arizona Press), p.3
- Woodward, P. R. 1976, ApJ, 207, 484
- Xu, J. & Stone, J. M. 1995, ApJ, 454, 172

Table 1. Model Parameters

| Model | n | χ | M | a_0/r_{co} | \mathcal{R} | $h_{\text{bd}}/r_{\text{co}}$ | $\langle \rho_{\text{cl}} \rangle / \rho_{i0}$ | Resolution |
|---------------------------|----------|--------|------|---------------------|---------------|-------------------------------|--|--|
| $\gamma = 5/3$, sphere | | | | | | | | |
| AS1 | 2 | 10 | 1.5 | 2.61 | 6.58 | 1.22 | 2.91 | R_{120} |
| AS2 | 2 | 10 | 10 | 2.61 | 6.58 | 1.22 | 2.91 | $R_{30}, R_{60}, R_{120}, R_{240}, R_{480}$ |
| AS3 | 2 | 10 | 100 | 2.61 | 6.58 | 1.22 | 2.91 | R_{120} |
| AS4 | 2 | 100 | 10 | 8.50 | 34.7 | 1.02 | 3.58 | R_{120} |
| AS5 | 4 | 10 | 10 | 1.49 | 1.91 | 0.611 | 4.01 | R_{120} |
| AS6 | 4 | 100 | 10 | 2.23 | 2.67 | 0.510 | 8.57 | R_{120} |
| AS7 | 8 | 10 | 1.5 | 1.15 | 1.23 | 0.306 | 5.62 | R_{120} |
| AS8 | 8 | 10 | 10 | 1.15 | 1.23 | 0.306 | 5.62 | $R_{30}, R_{60}, R_{120}, R_{240}, R_{480}, R_{960}$ |
| AS9 | 8 | 10 | 100 | 1.15 | 1.23 | 0.306 | 5.62 | R_{120} |
| AS10 | 8 | 10 | 1000 | 1.15 | 1.23 | 0.306 | 5.62 | R_{120} |
| AS11 | 8 | 100 | 10 | 1.27 | 1.28 | 0.255 | 23.0 | R_{120} |
| AS12 | 16 | 10 | 10 | 1.04 | 1.07 | 0.153 | 7.22 | R_{120} |
| AS13 | 24 | 10 | 10 | 1.02 | 1.03 | 0.102 | 7.97 | R_{120} |
| AS14 | ∞ | 10 | 10 | 1.00 | 1.00 | 0.00 | 10.0 | $R_{30}, R_{60}, R_{120}, R_{240}$ |
| AS15 | ∞ | 10 | 100 | 1.00 | 1.00 | 0.00 | 10.0 | R_{120} |
| AS16 | ∞ | 100 | 10 | 1.00 | 1.00 | 0.00 | 100.0 | R_{120} |
| $\gamma = 1.1$, sphere | | | | | | | | |
| IS1 | 2 | 10 | 10 | 2.61 | 6.58 | 1.22 | 2.91 | R_{120} |
| IS2 | 8 | 10 | 10 | 1.15 | 1.23 | 0.306 | 5.62 | R_{120} |
| $\gamma = 5/3$, cylinder | | | | | | | | |
| AC1 | 2 | 10 | 10 | 2.75 | 2.78 | 1.22 | 3.47 | R_{120} |
| AC2 | 8 | 10 | 10 | 1.25 | 1.11 | 0.306 | 6.59 | R_{120} |

Note. — In the eighth column, $\langle \rho_{\text{cl}} \rangle$ denotes the mean cloud velocity. In the sixth column, \mathcal{R} denotes the cloud mass normalized with $m_0 = 4\pi r_{\text{co}}^3 \rho_{c0} / 3$ and $\pi r_{\text{co}}^3 \rho_{c0}$ for spherical and cylindrical clouds, respectively. To estimate the cloud mass of a cylindrical cloud, we set the vertical height to be equal to the core radius r_{co} . In the last column, R_n means a grid resolution of n cells per core radius measured at the finest level of refinement (level 3).

Table 2. Dependence on n ($\chi = 10, M = 10, R_{120}$)

| Model Parameter | AS2 $n = 2$ | AS5 $n = 4$ | AS8 $n = 8$ | AS12 $n = 16$ | AS13 $n = 24$ | AS14 $n = \infty$ | | | | | |
|---|----------------|----------------|----------------|------------------|------------------|----------------------|-------|---------|-------|---------|-------|
| $t_{\text{slip}}/t_{\text{cc}}$ | 4.91 | 1.98 | 1.71 | 0.722 | 0.335 | 0.00 | | | | | |
| $t_{\text{drag}}/t_{\text{cc}}$ | 7.51 | 3.75 | 3.26 | 3.15 | 2.90 | 2.52 | | | | | |
| $t_{\text{dest}}/t_{\text{cc}}$ | 10.2 | 7.40 | 5.91 | 5.34 | 4.47 | 3.45 | | | | | |
| $t_{\text{mix}}/t_{\text{cc}}$ | 4.73 | 8.04 | 6.59 | 6.31 | 6.17 | 4.91 | | | | | |
| t_m/t_{cc} | 12.9 | 5.96 | 4.82 | 4.54 | 4.24 | 3.80 | | | | | |
| a/r_{co} | 3.04 | (3.08) | 2.07 | (1.98) | 1.73 | (1.66) | 1.75 | (1.75) | 1.76 | (1.75) | 2.21 |
| c/r_{co} | 3.45 | (2.67) | 1.85 | (1.05) | 1.48 | (1.29) | 1.62 | (1.51) | 1.79 | (1.75) | 1.63 |
| c/a | 1.12 | (0.865) | 0.893 | (0.529) | 0.855 | (0.775) | 0.928 | (0.862) | 1.02 | (0.998) | 0.738 |
| $\langle \rho \rangle / \langle \rho_0 \rangle$ | 2.55 | (1.59) | 2.20 | (1.97) | 1.90 | (1.84) | 1.65 | (1.59) | 1.48 | (1.42) | 1.24 |
| $\langle v_z \rangle / v_b$ | 0.173 | (0.124) | 0.182 | (0.186) | 0.200 | (0.206) | 0.173 | (0.170) | 0.162 | (0.162) | 0.130 |
| $\delta v_{\varpi} / v_b$ | 0.0758 | (0.0840) | 0.0953 | (0.0788) | 0.102 | (0.0840) | 0.113 | (0.105) | 0.116 | (0.113) | 0.115 |
| $\delta v_z / v_b$ | 0.0990 | (0.0703) | 0.0870 | (0.0701) | 0.158 | (0.119) | 0.164 | (0.159) | 0.181 | (0.176) | 0.182 |
| $-\Gamma / r_{\text{co}} v_b$ | 2.38 | | 0.501 | | 1.25 | | 1.20 | | 1.17 | | 1.50 |

Note. — All the time-dependent quantities are estimated at $t = t_m$. The initial cloud mass $m_{\text{cl},0}$ is adopted as the threshold mass in computing the global quantities, except that the values in parentheses are measured with respect to the initial core mass, $m_{\text{co},0}$. Note that the radii a and c are normalized by r_{co} . If the radius a is normalized by its initial value a_0 , then the radius of the shocked cloud decreases monotonically with n . See §4.3.

Table 3. Dependence on n ($\chi = 100, M = 10, R_{120}$)

| Model Parameter | AS4 $n = 2^a$ | AS6 $n = 4$ | AS11 $n = 8$ | AS16 $n = \infty$ | | | |
|---|------------------|----------------|-----------------|----------------------|-------|----------|--------|
| $t_{\text{slip}}/t_{\text{cc}}$ | 3.50 | 1.63 | 1.10 | 0.00 | | | |
| $t_{\text{drag}}/t_{\text{cc}}$ | 10.5 | 5.22 | 5.01 | 3.59 | | | |
| $t_{\text{dest}}/t_{\text{cc}}$ | 12.1 | 6.51 | 6.50 | 3.02 | | | |
| $t_{\text{mix}}/t_{\text{cc}}$ | 12.0 | 6.24 | 5.69 | 4.72 | | | |
| t_m/t_{cc} | > 15.0 | 7.05 | 6.57 | 4.01 | | | |
| a/r_{co} | 8.14 | (0.385) | 3.42 | (1.91) | 3.16 | (2.83) | 3.15 |
| c/r_{co} | 26.6 | (4.45) | 15.3 | (3.41) | 11.2 | (9.50) | 3.15 |
| c/a | 3.27 | (11.5) | 4.48 | (1.79) | 3.57 | (3.35) | 2.65 |
| $\langle \rho \rangle / \langle \rho_0 \rangle$ | 2.01 | (0.240) | 0.959 | (0.390) | 0.245 | (0.289) | 2.65 |
| $\langle v_z \rangle / v_b$ | 0.239 | (0.286) | 0.181 | (0.314) | 0.184 | (0.217) | 0.240 |
| $\delta v_{\varpi} / v_b$ | 0.0571 | (0.0582) | 0.0810 | (0.0418) | 0.102 | (0.0840) | 0.0987 |
| $\delta v_z / v_b$ | 0.142 | (0.0989) | 0.0870 | (0.0701) | 0.175 | (0.106) | 0.236 |
| $-\Gamma / r_{\text{co}} v_b$ | 17.0 | | 10.4 | | 8.03 | | 6.51 |

^aThe time-dependent quantities are evaluated at $t = 16.2 t_{\text{cc}}$.

Note. — The time-dependent values are estimated at $t = t_m$. The initial cloud mass $m_{\text{cl},0}$ is adopted as the threshold mass to compute the global quantities, except in the values in parentheses which are the global quantities measured in the initial core mass, $m_{\text{co},0}$.

Table 4. Dependence on M ($\chi = 10, R_{120}$)

| Parameter | $n = 8^a$ | | | | | | $n = 2$ | | | | | |
|---|-----------|----------|-------|----------|-------|----------|---------|----------|--------|----------|--------|----------|
| Model | AS7 | AS9 | AS10 | AS1 | AS2 | AS3 | AS7 | AS9 | AS10 | AS1 | AS2 | AS3 |
| M | 1.5 | 100 | 1000 | 1.5 | 10 | 100 | | | | | | |
| v_{c0}/v_b | 0.417 | 0.750 | 0.750 | 0.417 | 0.742 | 0.750 | | | | | | |
| $t_{\text{drag}}/t_{\text{cc}}$ | 17.2 | 3.25 | 3.25 | 21.4 | 7.51 | 6.92 | | | | | | |
| $t_{\text{dest}}/t_{\text{cc}}$ | 12.2 | 5.88 | 5.87 | 32.8 | 10.2 | 10.1 | | | | | | |
| $t_{\text{mix}}/t_{\text{cc}}$ | 15.8 | 6.52 | 6.60 | 25.1 | 4.73 | 4.92 | | | | | | |
| t_m/t_{cc} | 7.51 | 5.15 | 5.13 | > 32.7 | 12.9 | 13.6 | | | | | | |
| a/r_{co} | 1.82 | (1.74) | 1.80 | (1.71) | 1.80 | (1.78) | 3.89 | (4.02) | 3.04 | (3.08) | 3.18 | (3.24) |
| c/r_{co} | 1.49 | (1.18) | 1.60 | (1.48) | 1.60 | (1.50) | 5.20 | (4.39) | 3.45 | (2.67) | 3.46 | (2.32) |
| c/a | 0.816 | (0.680) | 0.889 | (0.864) | 0.888 | (0.845) | 1.34 | (1.09) | 1.12 | (0.865) | 1.09 | (0.716) |
| $\langle \rho \rangle / \langle \rho_0 \rangle$ | 1.33 | (1.37) | 1.86 | (1.70) | 1.86 | (1.72) | 1.25 | (0.712) | 2.55 | (1.59) | 2.55 | (1.50) |
| $\langle v_z \rangle / v_b$ | 0.193 | (0.197) | 0.182 | (0.193) | 0.182 | (0.193) | 0.114 | (0.0904) | 0.173 | (0.124) | 0.159 | (0.125) |
| $\delta v_{\varpi} / v_b$ | 0.0629 | (0.0508) | 0.104 | (0.0900) | 0.104 | (0.0908) | 0.0475 | (0.0410) | 0.0758 | (0.0840) | 0.0781 | (0.0732) |
| $\delta v_z / v_b$ | 0.0879 | (0.0646) | 0.172 | (0.146) | 0.164 | (0.140) | 0.0738 | (0.0654) | 0.0990 | (0.0703) | 0.101 | (0.0711) |
| $-\Gamma / r_{\text{co}} v_b$ | 1.55 | 1.22 | 1.22 | 2.23 | 2.38 | 2.37 | | | | | | |

^asee Table 2 for the global quantities of $\chi = 10$

Note. — The time-dependent values are estimated at $t = t_m$. The initial cloud mass $m_{\text{cl},0}$ is adopted as the threshold mass to compute the global quantities, except in the values in parentheses which are the global quantities measured in the initial core mass, m_{co} .

Table 5. Radiative Clouds ($\chi = 10, M = 10, R_{120}$)

| Model | IS1 | IS2 | | |
|---|---------|----------|--------|----------|
| Parameter | $n = 2$ | $n = 8$ | | |
| $t_{\text{drag}}/t_{\text{cc}}$ | 0.500 | 1.56 | | |
| $t_{\text{dest}}/t_{\text{cc}}$ | 7.23 | 6.71 | | |
| $t_{\text{mix}}/t_{\text{cc}}$ | 6.10 | 5.56 | | |
| t_m/t_{cc} | > 8.87 | 4.99 | | |
| a/r_{co} | 2.41 | (1.29) | 1.11 | (0.830) |
| c/r_{co} | 6.74 | (8.19) | 4.54 | (3.20) |
| c/a | 2.79 | (6.36) | 1.15 | (3.86) |
| $\langle \rho \rangle / \langle \rho_0 \rangle$ | 10.8 | (6.12) | 7.05 | (5.65) |
| $\langle v_z \rangle / v_b$ | 0.129 | (0.0649) | 0.164 | (0.196) |
| $\delta v_{\varpi} / v_b$ | 0.0541 | (0.0500) | 0.0553 | (0.0532) |
| $\delta v_z / v_b$ | 0.0989 | (0.149) | 0.106 | (0.0793) |
| $-\Gamma / r_{\text{co}} v_b$ | 0.140 | 0.327 | | |

Note. — We note that the circulation associated with the supersonic vortex ring, normalized with $r_{\text{co}} v_b$, contributes more for radiative clouds than for nonradiative clouds. Since this has the opposite sign from the other contributions to the circulation, the values for the total circulation listed above are smaller than those in Table 2. However, the peak values of the circulation are close to those of the nonradiative cases.

Table 6. Cylindrical Clouds ($\chi = 10, M = 10, R_{120}$)

| Model Parameter | AC1 $n = 2^a$ | AC2 $n = 8$ |
|---|------------------|-----------------|
| $t_{\text{drag}}/t_{\text{cc}}$ | 2.04 | 2.38 |
| $t_{\text{dest}}/t_{\text{cc}}$ | 17.1 | 6.25 |
| $t_{\text{mix}}/t_{\text{cc}}$ | 18.7 | 11.3 |
| t_m/t_{cc} | > 19.0 | 9.14 |
| a/r_{co} | 3.43 (3.53) | 2.23 (2.23) |
| c/r_{co} | 3.00 (2.84) | 3.24 (3.15) |
| c/a | 0.876 (0.805) | 1.45 (1.41) |
| $\langle \rho \rangle / \langle \rho_0 \rangle$ | 2.46 (2.00) | 1.50 (1.37) |
| $\langle v_z \rangle / v_b$ | 0.0915 (0.0975) | 0.111 (0.111) |
| $\delta v_{\varpi} / v_b$ | 0.0758 (0.0635) | 0.0893 (0.0893) |
| $\delta v_z / v_b$ | 0.0885 (0.0662) | 0.136 (0.136) |
| $-\Gamma / r_{\text{co}} v_b$ | 2.03 | 2.24 |

^aFor $n = 2$, the time-dependent global quantities are evaluated at $t = 12.9 t_{\text{cc}}$, which is the maximum expansion time for the spherical case.

Note. — The time-dependent values are estimated at $t = t_m$. The initial cloud mass $m_{\text{cl},0}$ is adopted as the threshold mass to compute the global quantities, except in the values in parentheses which are the global quantities measured in the initial core mass, m_{co} .

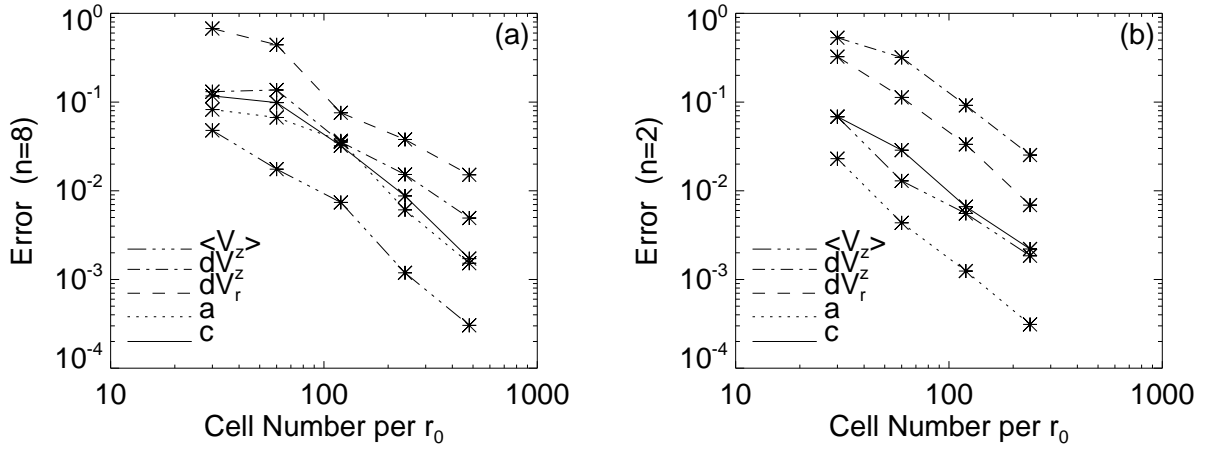


Fig. 1.— Results of convergence studies for (a) $(n, \chi, M) = (8, 10, 10)$ and (b) $(2, 10, 10)$. The ordinate denotes the relative error, while the abscissa denotes the number of grid cells per radius, which is a measure of the spatial resolution. See the text for the definition of the relative errors. The global quantities are compared at $t = 3t_{cc}$ and $6t_{cc}$ for $n = 8$ and 2, respectively.

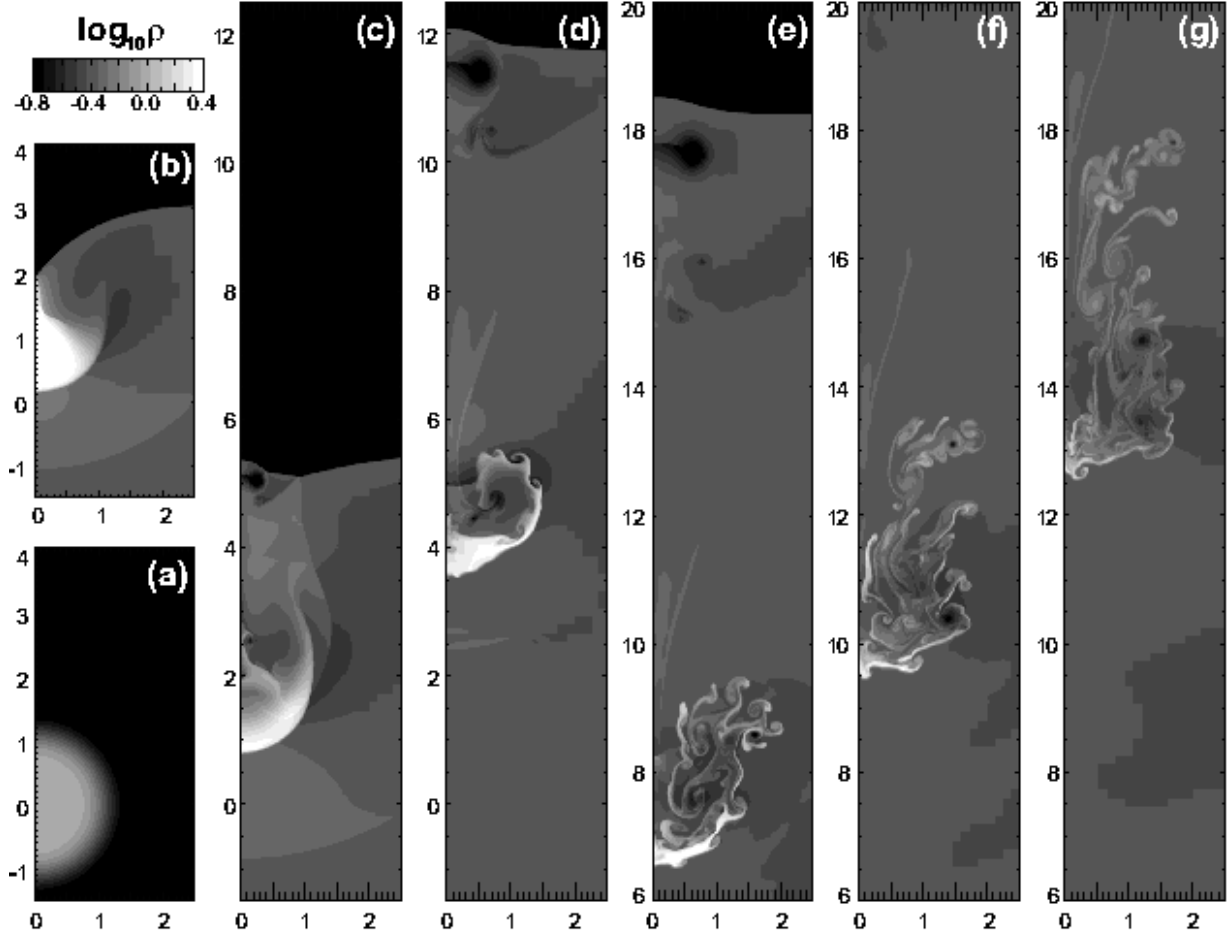


Fig. 2.— Snapshots of the density distribution for model AS8 with $n = 8$, $\chi = 10$, and $\gamma = 5/3$ interacting with a strong shock of $M = 10$ at seven different times: (a) initial state ($t = -0.39 t_{cc}$), (b) $1.24 t_{cc}$, (c) $2.00 t_{cc}$, (d) $4.00 t_{cc}$, (e) $6.00 t_{cc}$, (f) $8.00 t_{cc}$, and (g) $10.00 t_{cc}$, where the evolution time is measured from the stage at which the shock has reached at $z/r_{co} = -1$ on the z -axis. The abscissa and ordinate denote the ϖ - and z -coordinates, respectively, normalized by the core radius, r_{co} . The initial planar shock was initiated at $z/r_{co} = -2.1$. The arch-like density jump appearing at $z/r_{co} \sim -1$ and -0.85 in panels (b) and (c), respectively, is a bow shock, which is formed by the shock reflected at the cloud surface. The black spot appearing at $(\varpi/r_{co}, z/r_{co}) \sim (0.2, 5)$ in panel (c) is a supersonic vortex ring, which propagates, with almost the same speed as the intercloud shock, up to $(\varpi/r_{co}, z/r_{co}) \simeq (0.5, 11.4)$ and $(0.6, 17.6)$ in panels (d) and (e), respectively.

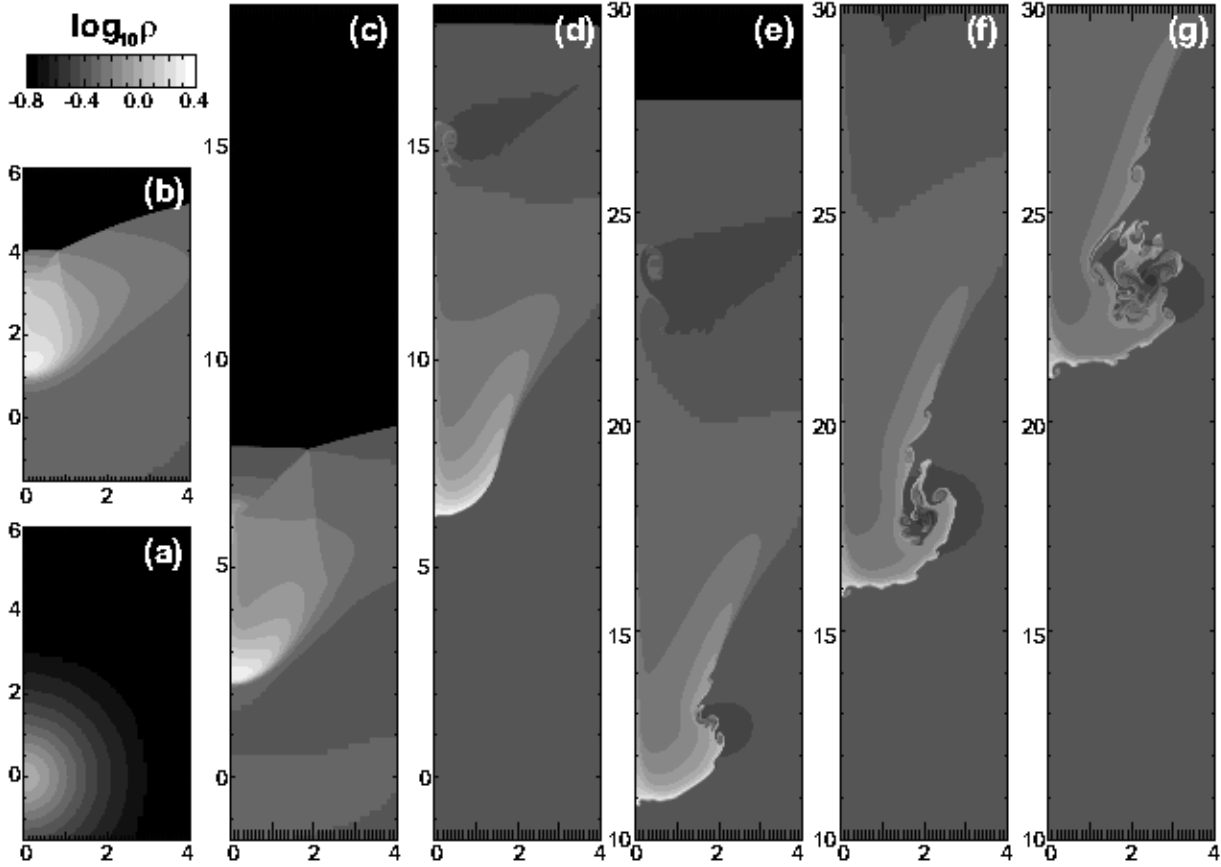


Fig. 3.— Snapshots of the density distribution for model AS2 with $n = 2$, $\chi = 10$, and $\gamma = 5/3$ interacting with a shock of $M = 10$ at seven different times: (a) initial state ($t = -5.76 t_{cc}$), (b) $1.93 t_{cc}$, (c) $3 t_{cc}$, (d) $6 t_{cc}$, (e) $9 t_{cc}$, (f) $12 t_{cc}$, and (g) $15 t_{cc}$, where the evolution time is measured from the stage at which the shock has reached at $z/r_{co} = -1$ on the z -axis. The initial planar shock was initiated at $z/r_{co} = -18$.

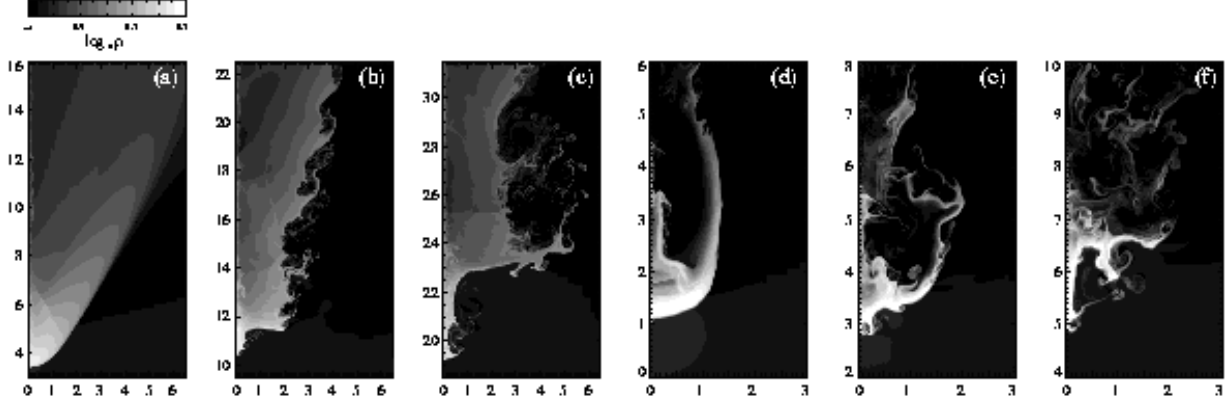


Fig. 4.— (a), (b), and (c): Snapshots of the density distribution for model AS4 with $(n, \chi, M) = (2, 100, 10)$ at (a) $t = 3t_{cc}$, (b) $t = 6t_{cc}$, and (c) $t = 9t_{cc}$. (d), (e), and (f): Snapshots of the density distribution for model AS11 with $(n, \chi, M) = (8, 100, 10)$ at (d) $t = 2t_{cc}$, (e) $t = 4t_{cc}$, and (f) $t = 6t_{cc}$.

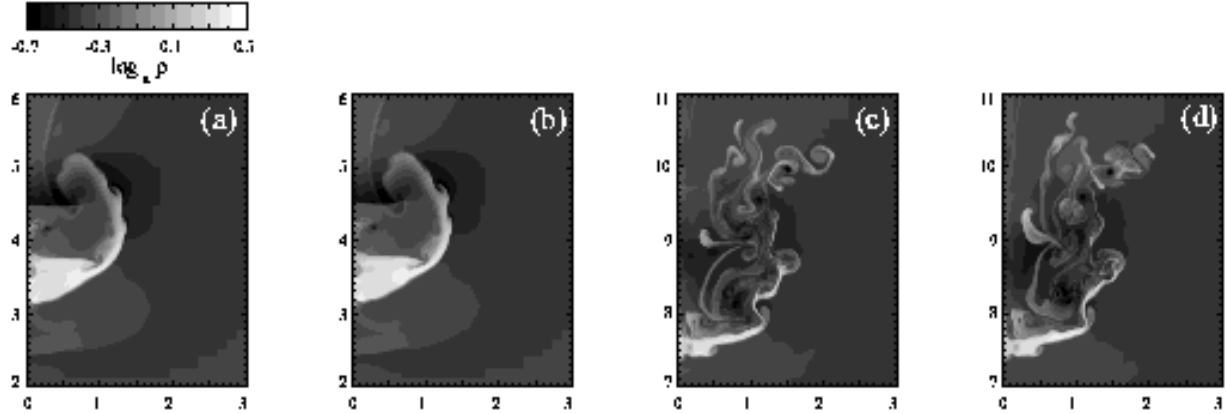


Fig. 5.— Mach scaling. Comparison of the density distributions between models AS8 and AS9 with $n = 8$ and $\chi = 10$: (a) model AS9 ($M = 100$) at $t = 3.5t_{cc}$, (b) model AS10 ($M = 1000$) at $t = 3.5t_{cc}$, (c) model AS9 ($M = 100$) at $t = 6.4t_{cc}$, (d) model AS10 ($M = 1000$) at $t = 6.4t_{cc}$. The morphology of the cloud is remarkably similar at the first time, whereas small differences in the small-scale structures begin to appear at the second time. Note that the global quantities agree very well even at the later times (see the text for more detail).

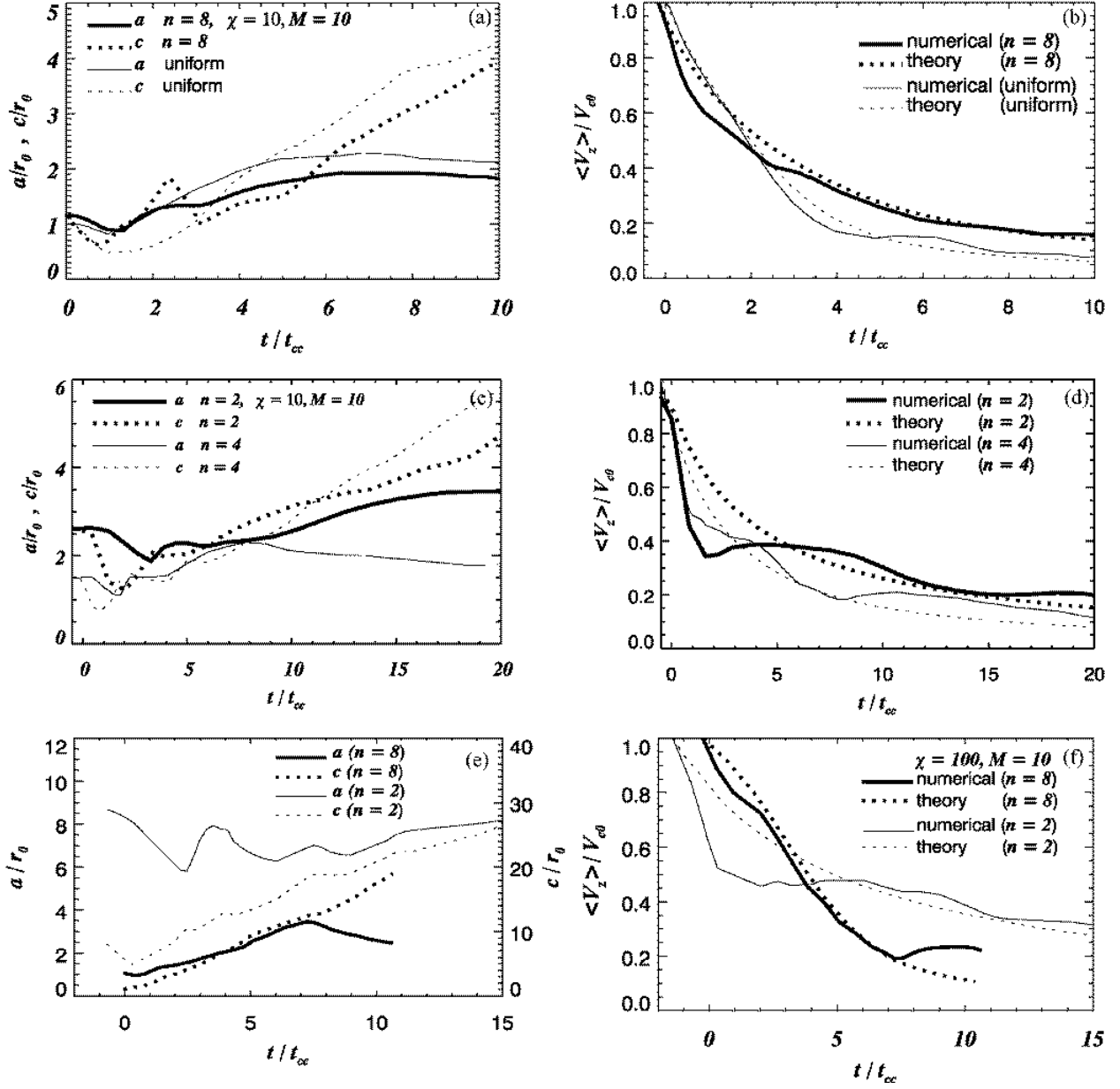


Fig. 6.— (a) and (b): Time evolution of the cloud shape and the cloud velocity for two different models with $(n, \chi, M) = (8, 10, 10)$ (*thick curves*) and $(\infty, 100, 10)$ (*thin curves*). Panel (a) shows the time evolution of the rms radial radius a (*solid curves*) and axial radius c (*dotted curves*). Panel (b) shows the time evolution of the mean cloud velocity (*solid curves*). For comparison, the analytic solution is indicated by *dotted curves*. (c) and (d): Same as the upper panels but for the models with $(n, \chi, M) = (2, 10, 10)$ and $(4, 10, 10)$. (e) and (f): Same as the upper panels but for the models with

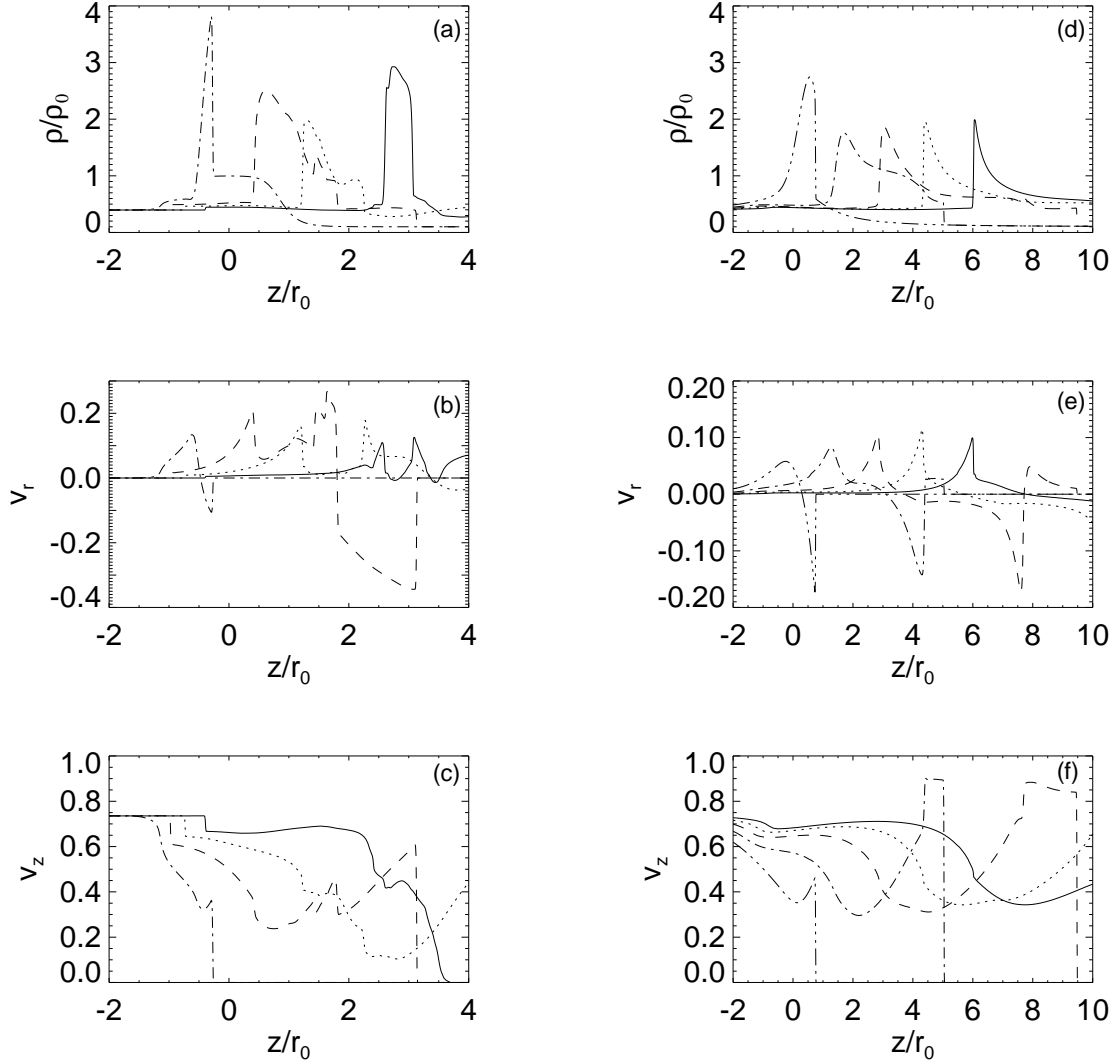


Fig. 7.— Distributions of (a) density, (b) v_r , and (c) v_z , along $r = 0.5 r_{co}$, for $n = 8$, $\chi = 10$, and $M = 10$. Solid, dotted, dashed, and dash-dot curves indicate the profiles at $t = 0.249 t_{cc}$, $1.31 t_{cc}$, $2.13 t_{cc}$, and $3.04 t_{cc}$, respectively. Distributions of (d) density, (e) v_r , and (f) v_z , along $r = 0.5 r_{co}$, for $n = 2$, $\chi = 10$, and $M = 10$. Solid, dotted, dashed, dash-dot, and dash-dot-dot-dot curves indicate the profiles at $t = 1.49 t_{cc}$, $2.82 t_{cc}$, $4.05 t_{cc}$, $5.18 t_{cc}$, and $6.41 t_{cc}$, respectively.

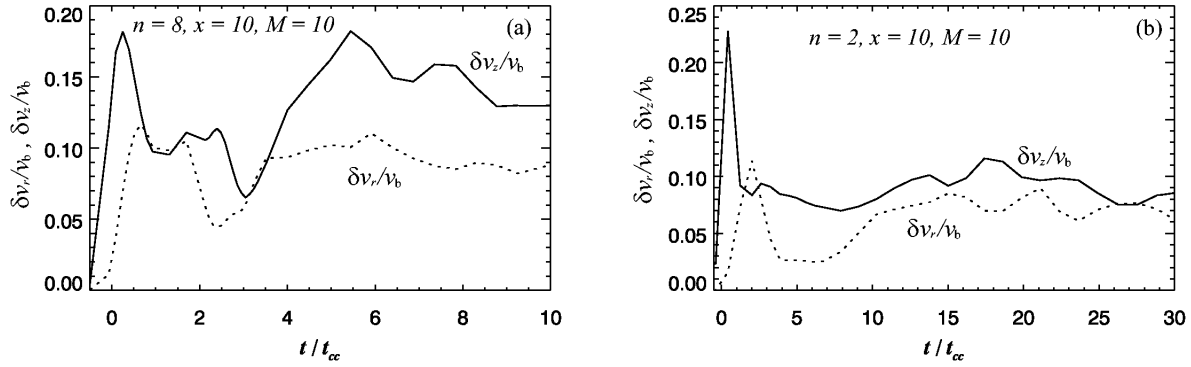


Fig. 8.— Time evolution of the radial (dotted curve) and axial (solid curve) velocity dispersions for (a) $n = 8$, $\chi = 10$, and $M = 10$ and (b) $n = 2$, $\chi = 10$, and $M = 10$.

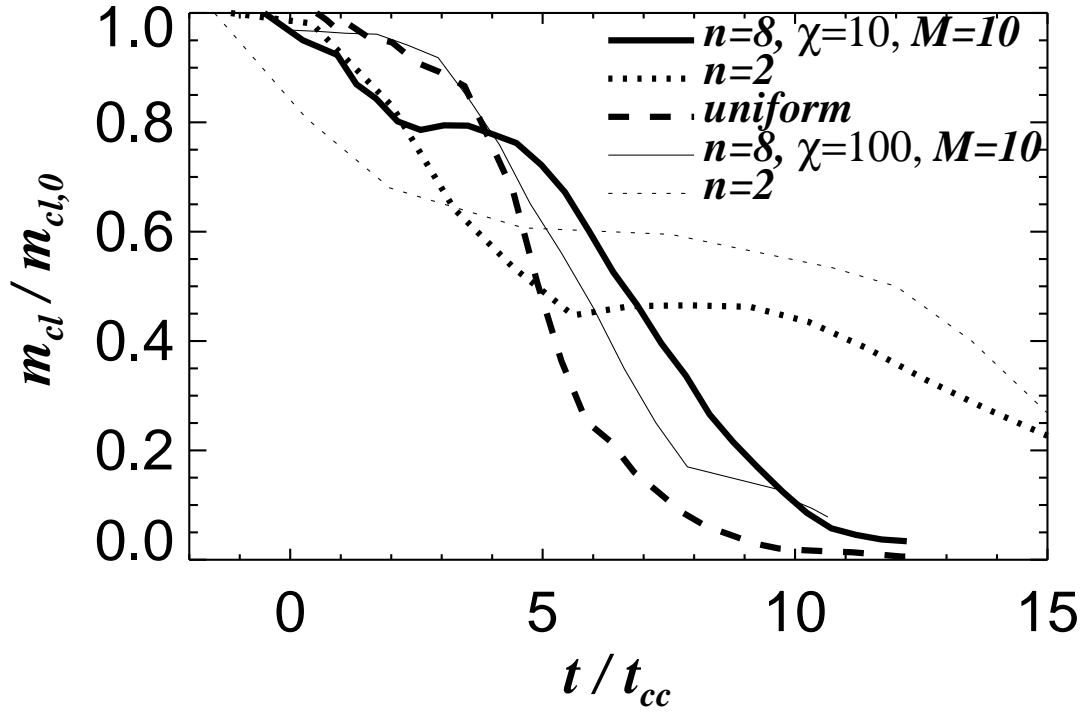


Fig. 9.— Time evolution of fractional masses with densities greater than $2 \rho_{11}$, normalized by the initial cloud mass.

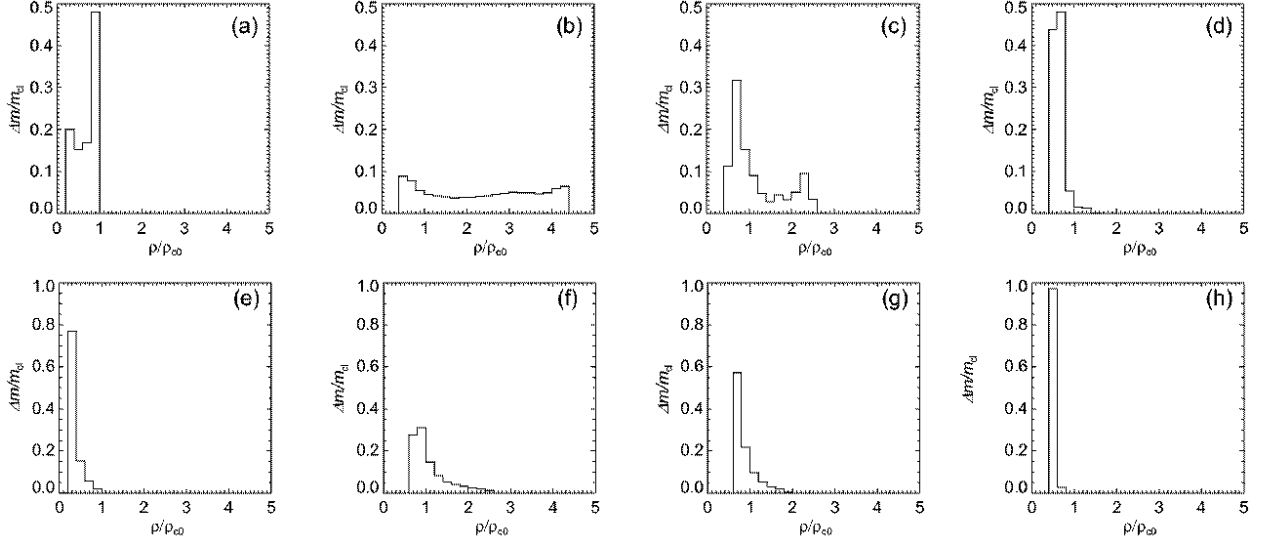


Fig. 10.— Evolution of the mass fraction for the models with $(n, \chi, M) = (8, 10, 10)$ at times (a) $t = 0$, (b) $1.06 t_{cc}$, (c) $6.04 t_{cc}$, and (d) $8.00 t_{cc}$, and for the models with $(n, \chi, M) = (2, 10, 10)$ at times (e) $t = 0$, (f) $1.40 t_{cc}$, (g) $7.28 t_{cc}$, and (h) $29.5 t_{cc}$. The histograms indicate the fraction of mass contained within a corresponding density bin with a width of $0.2 \rho_{c0}$, which is normalized by the total cloud mass $m_{cl,0}$.

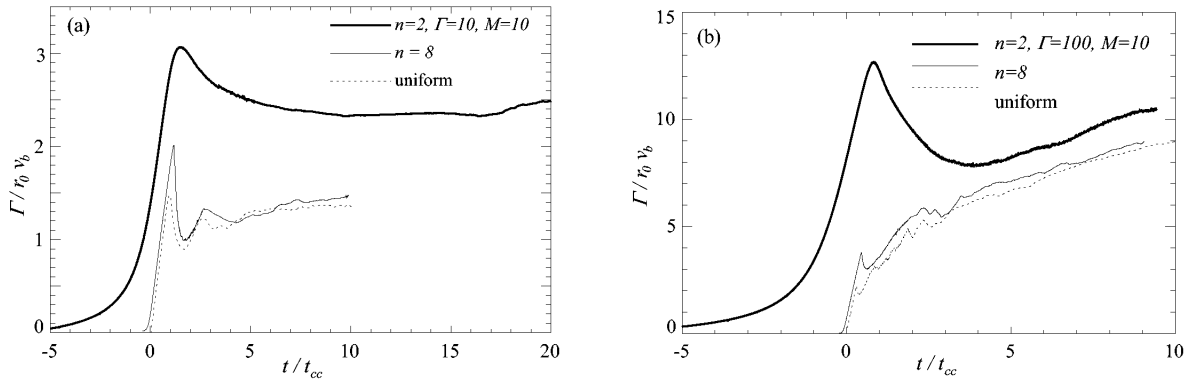


Fig. 11.— Time evolution of circulations for clouds with (a) $\chi = 10$ and clouds with (b) $\chi = 100$. Thick solid, thin solid, and dashed curves denote the time evolution of the total circulation for the models with $n = 2, 8$, and ∞ , respectively.

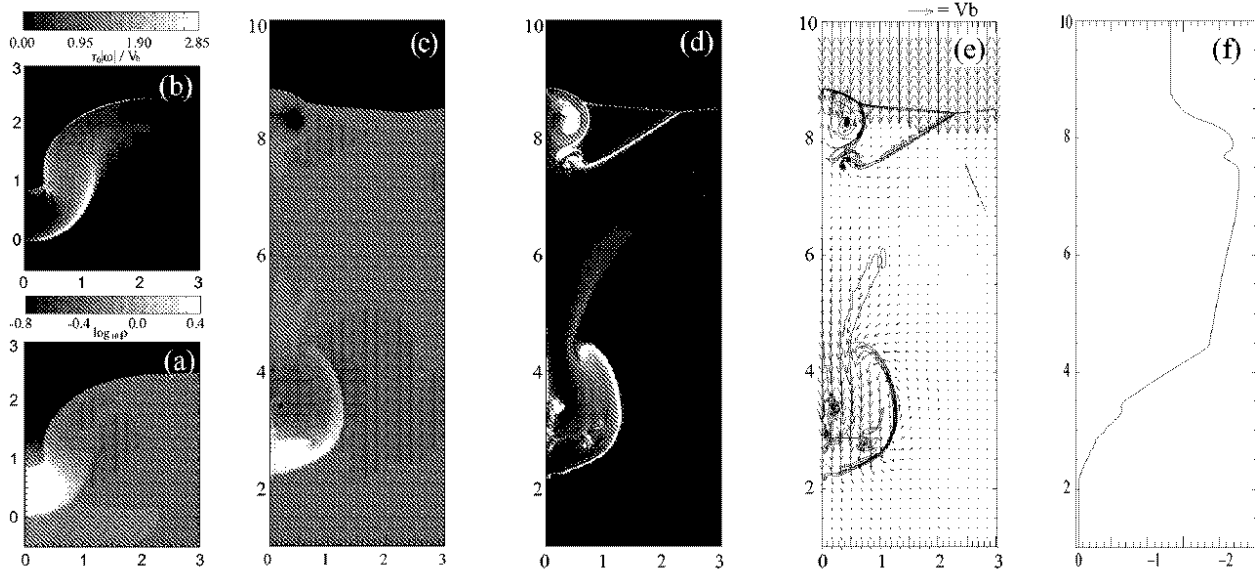


Fig. 12.— Density and vorticity distributions for the model with $(n, \chi, M) = (8, 10, 10)$. Panels (a) and (b): the density distribution and vorticity distribution at $t = 0.930 t_{cc}$. Panels (c), (d), and (e): the density distribution, vorticity distribution, and the velocity distribution at $t = 2.86 t_{cc}$. The velocity vectors are measured in the frame that moves with the postshock flow. Panel (f): cumulative circulation at $t = 2.86 t_{cc}$.

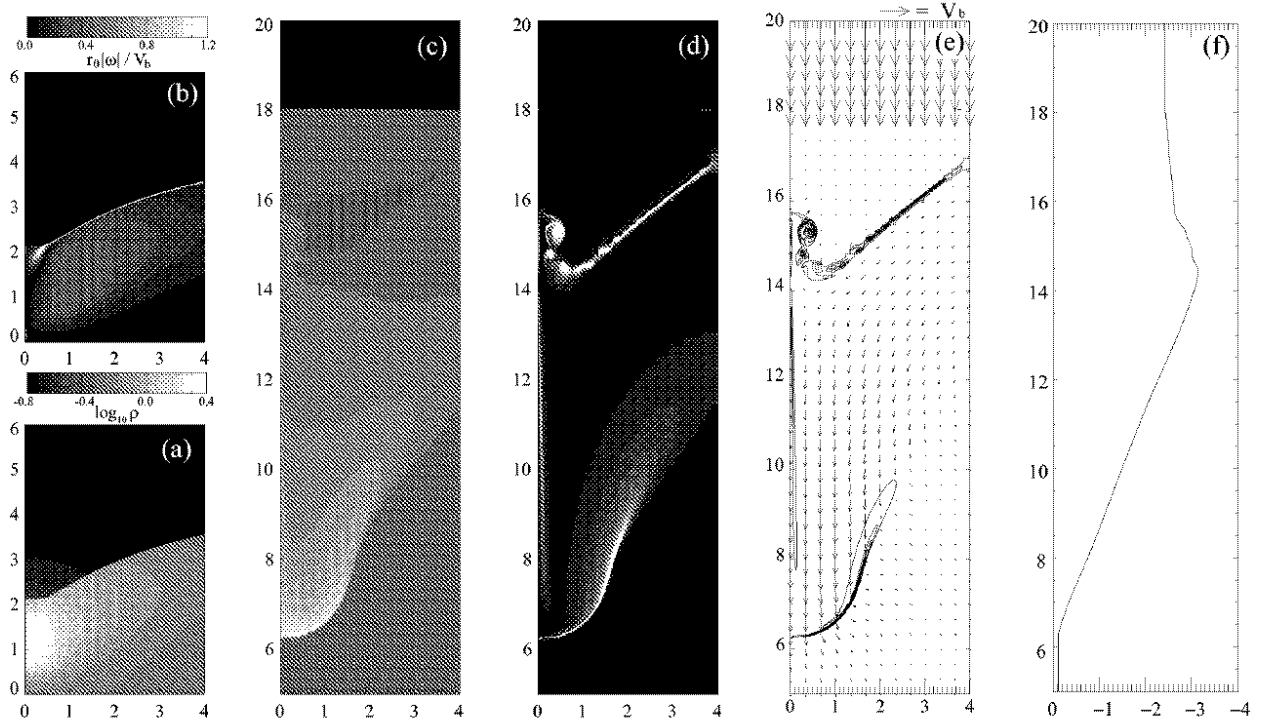


Fig. 13.— Density and vorticity distributions for the model with $(n, \chi, M) = (2, 10, 10)$. Panels (a) and (b): the density distribution and vorticity distribution at $t = 2.02 t_{cc}$. Panels (c), (d), and (e): the density distribution, vorticity distribution, and the velocity distribution at $t = 6.65 t_{cc}$. The velocity vectors are measured in the frame that moves with the postshock flow. Panel (f): cumulative circulation at $t = 6.65 t_{cc}$.

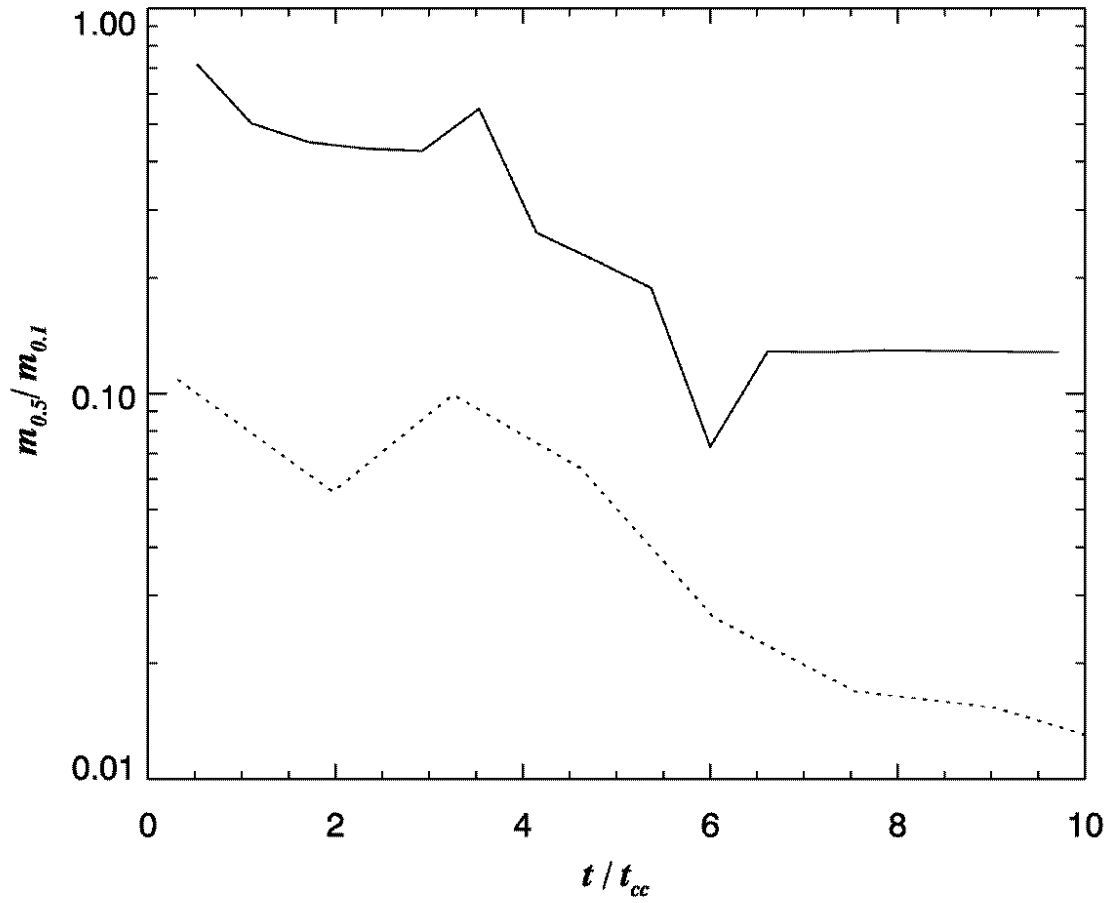


Fig. 14.— Evolution of the mass ratio for the models with $(n, \chi, M) = (8, 100, 10)$ and $(2, 100, 10)$, which are plotted with solid and dotted curves, respectively.

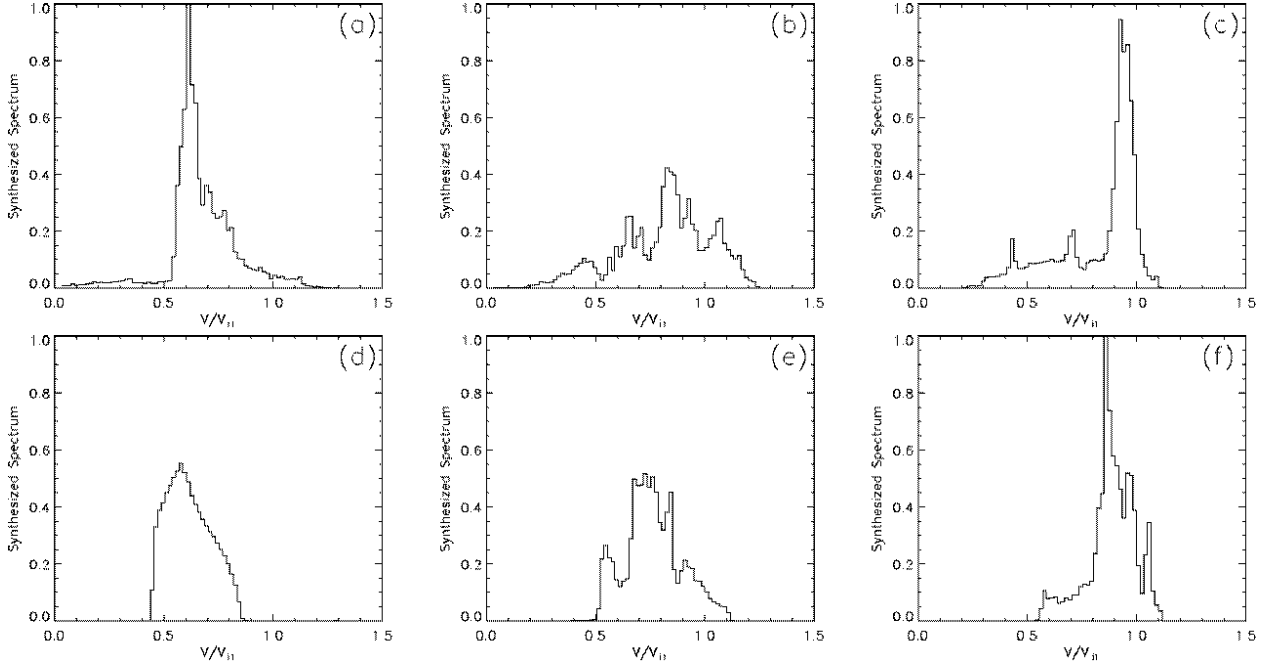


Fig. 15.— Synthesized spectra for the model with $(n, \chi, M) = (8, 10, 10)$ at (a) $t = 4.00 t_{cc}$, (b) $8.00 t_{cc}$, and (c) $13.2 t_{cc}$, and for the model with $(n, \chi, M) = (2, 10, 10)$ at (d) $t = 6.00 t_{cc}$, (e) $12.0 t_{cc}$, and (f) $20.1 t_{cc}$. The spectra are normalized by the maximum at (a) and (d) for $n = 8$ and 2, respectively. The histograms denote the mass contained within a corresponding velocity bin with a width of $0.015 v_{i1}$. The abscissa denotes the velocity normalized by the velocity of the postshock ambient medium v_{i1} . The integration is done over the entire cloud under the assumption that the line-of-sight is parallel to the z -axis.

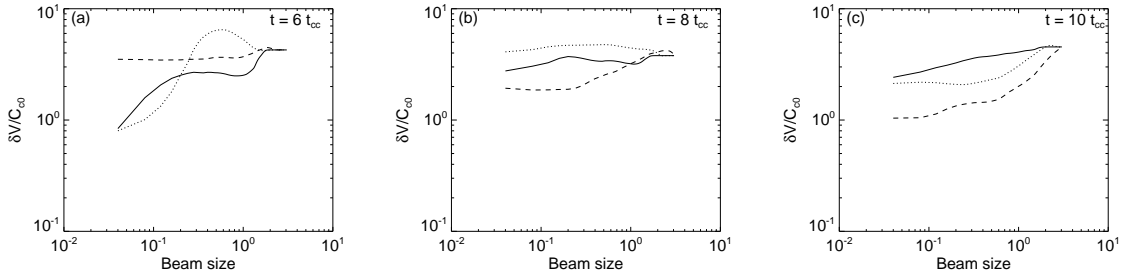


Fig. 16.— linewidth-size relation in shocked clouds with $(n, \chi, M) = (8, 10, 10)$ at three different times: (a) $t = 6 t_{cc}$, (b) $8 t_{cc}$, and (c) $10 t_{cc}$. This model is followed with the three-dimensional simulation with an intermediate resolution R_{60} . The abscissa denotes the beam size, while the ordinate is the velocity dispersion estimated in the beam with a size R . The velocity dispersions are measured in units of the sound speed at the center of the preshock cloud, C_{c0} . Solid curves show the velocity dispersions measured from the direction whose line-of-sight is identical to the z -axis. Dotted and dashed curves show the velocity dispersions measured from the direction whose line-of-sight is perpendicular to the z -axis. For dotted and dashed curves, the beam center is put on the center of gravity, z_G , and $z_G + r_{co}$, respectively.